Dynamics of Shape and Composition of an Active Composite Membrane

by

Kripa G

Thesis submitted to the Jawaharlal Nehru University for the degree of Doctor of Philosophy

2009

Contents

Chapter 1

Introduction

1.1 The Surface of the Cell

The cell is a machine, using food to convert chemical energy for the various processes it requires for its running. New pieces of information about the sub-processes that keep the cell functioning are discovered everyday, along with a growing number of molecular players. The cell has evolved both a spatial compartmentalization, and a functional modularity, and it is evident that these two properties are highly correlated. The membrane bound Golgi apparatus, for instance, is mainly concerned with the sorting of proteins; the endoplasmic reticulum, with the production of proteins. The general consensus is that such spatial localization of function aids in the orchestration of a large number of events.

The plasma membrane is highly dynamic and has a range of functions as well. On account of being the physical barrier between the cytosol and the extracellular medium, it forms the via media for cross talk between the two. One can easily see that the plasma membrane *must* have the following properties: (1) It must be a highly selective barrier, capable of allowing molecules with a range of sizes, into the cell (2) It must be capable of transmitting information across. It is therefore quite conceivable that the plasma membrane has evolved a spatial organization similar in principle to the three dimensional cell, to perform these functions efficiently.

We explore the possible general routes that can enable "compartmentalization" on the membrane. The presence of physical barriers in the most obvious route. Analogous to the role the membrane plays in the 3D structure of the cell, the barriers can prevent

or restrict diffusion between different membrane regions. As illustrations of different mechanisms, we use three examples: (1) The clathrin coated pit (2) The cytoskeletal meshwork (3) Heterogeneities in the lipids.

1.1.1 Example 1: The Clathrin Coated Pit

Heterogeneity is highlighted at the plasma membrane during the process of clathrin-mediated endocytosis [1](Figure 1.1). Many large particles, like the LDL (Low Density Lipoprotein), enter the cell by first binding to a transmembrane receptor (the LDL receptor). The transmembrane receptor straddles both the leaves of the bilayer plasma membrane, and hence is physically connected to both the outside and inside of the cell. The cargo-receptor binding initiates further binding of a clathrin monomer, on the cytosolic side of the transmembrane receptor. On polymerization, clathrin has the ability to further cluster together cargo bound receptors. Polymerized clathrin forms a fully enclosed cage, and is eventually pinched off from the membrane by the action of dynamin, an ATP hydrolyzing machine. The agent leading to the transient heterogeneity in this case is the clathrin coated pit. Other pathways that make use of clathrin-like proteins, like COP-I, COP-II, are also found on the membranes of internal organelles like the Golgi, and are similar in principle to the clathrin mediated pathway. It is a pathway which is triggered by the cargo-receptor binding, and hence these heterogeneities are *induced*.

1.1.2 Example 2: The Cytoskeletal Meshwork

The cell cortex, can also act as a physical barrier. Interlinked actin filaments form a dense meshwork just below the plasma membrane. Morone et al [32]constructed a 3 dimensional tomography (Figure 1.2) of a ripped off piece of plasma membrane, along with the cortical actin adjacent to it. The images reveal that actin is aligned mostly horizontal to the membrane, forming a meshwork of typical meshsize ranging from 30 nm to 300 nm (in rat kidney cells ; size may vary with cell type). Single molecule tracking of immuno-gold labeled surface molecules at a very high time resolution (25 microsecond) by the same lab [43], concluded that molecules perform fast thermal diffusion within, and slower hop diffusion in between compartments, whose size distribution matches that of the cortical actin mesh. Recent Fluorescence Correlation Spectroscopy (FCS) measurements from our lab (unpublished material) also show two kinds of diffusive behaviour, a fast

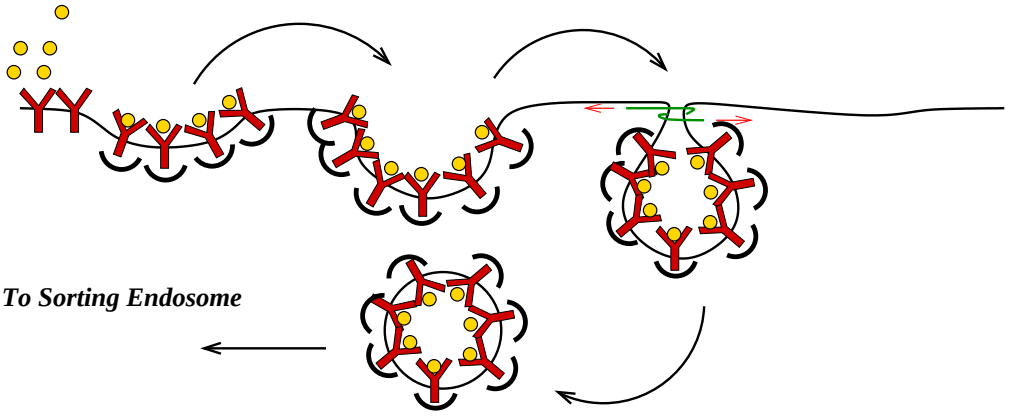

Figure 1.1: **Clathrin mediated endocytosis:** Clathrin and Dynamin dependent pathway: Trans-membrane cargo receptors (in maroon) bind to cargo (in gold) resulting in the binding of a clathrin "cap" (in black). Subsequently, bound receptors are brought together to form a fully enclosed vesicle. This vesicle is pinched off from the plasma membrane due to the ATP driven pinching action of Dynamin (in green). These vesicles are then taken to the Sorting endosome

diffusion, and a slow diffusion, whose amplitudes and values dependent on the molecule, and the cell type (and hence the mesh size).

Qualitatively, the two kinds of diffusion seem to be independent of the nature of the tagged molecule: they could be upper or lower leaflet lipids or proteins, all the molecules feel the effect of the actin meshwork. The interactions of membrane molecules and the cytoskeleton are yet uncharacterized. They could arise from steric hindrance or scale dependent hydrodynamic dissipation of membrane molecules, however these properties are derivable from the the static properties of the meshwork: they *need not* depend on its dynamics.

1.1.3 Example 3: Lipid Heterogeneities

The two instances cited so far both assume that the environment in which diffusion, or sequestering, of molecules takes place is a passive player, merely acting as a source of fluctuations and a sink of dissipation. This is the basis of the Fluid Mosaic model of Singer and Nicholson [1], which likens the plasma membrane to an artificial multicomponent membrane. In the fluid mosaic, it is possible that a few the molecules associate with each other to form energetically favourable configurations. In particular, Cholesterol and Sphingolipids are shaped such that their packing maximizes Van Der Waals Interactions,

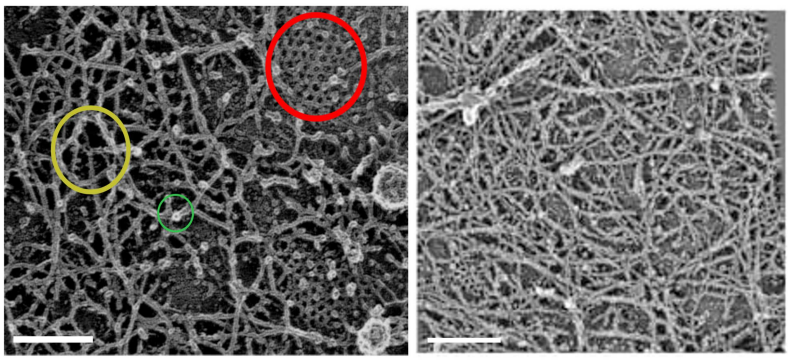

Figure 1.2: **Cortical Actin Meshwork.** Two dimensional projections of a cryo electron micrograph of the underside of the membrane. Left Panel: Normal rat kidney fibroblasts. Attached to the membrane are found (1) Clathrin Coated Pits (red circle), (2) A meshwork mostly horizontal to the membrane (brown circle) (2) Filaments of actin pointing towards the membrane (green circle). The mean mesh size is ∼230 nm. Right panel: Fetal rat skin keratocytes, with a much small mesh size ∼50 nm(Courtesy Morone et al, http://www.nanobio.frontier.kyoto-u.ac.jp/lab/slides/4/e.html)(Scale bar = 200 nm)

at a cost to entropy. Cholesterol, a small almost planar molecule with a very small headgroup, occupies the interstices in between sphingolipids, that have long saturated fatty acid chains and a large head group. This arrangement is energetically favourable as it maximizes interactions between the polar groups of the lipids. Fluorescence imaging of Giant Unilamellar vesicles (GUVs) (Figure 1.3 (b)) containing appropriate proportions of cholesterol, saturated lipids (DPPC) and other unsaturated lipids (DOPC), do show large phase segregated domains rich in cholesterol and sphingolipids, separated from the unsaturated lipids (green) [21]. When phase segregation occurs, the long saturated tails of the sphingolipids increases the local thickness of the membrane, such a region of low entropy and low energy is referred to as the Liquid Ordered phase, and coexists on artificial membranes, with the liquid disordered phase made up of short, unsaturated lipids. Single molecule tracking measurements show that the diffusion constant is much larger in the LD phase than in the LO phase. The phase diagram at 23^oC (Figure 1.3 (a)) for such a ternary mixture (cholesterol + PSM (unsaturated lipid) + POPC (saturated lipid)), reflects the coexistence of the LO and the LD phases at certain proportions of the three. The mole fractions of the three species are plotted along the three sides of the triangle, reaching 100% at the vertices. In the coexistence region, as the cholesterol percentage increases from 10% to 35%, the size of the LO domains in the co-existence

region progressively increases from nanometers to the order of microns.

The plasma membrane contains a large amount of cholesterol (∼40 %) and sphingolipids (∼20 %). In order for the above mechanism to be a candidate for lipid- based heterogeneities, the cell is expected to be in the coexistence regime of the phase diagram, corresponding to micron sized domains. However, this has not been detected in the plasma membrane.

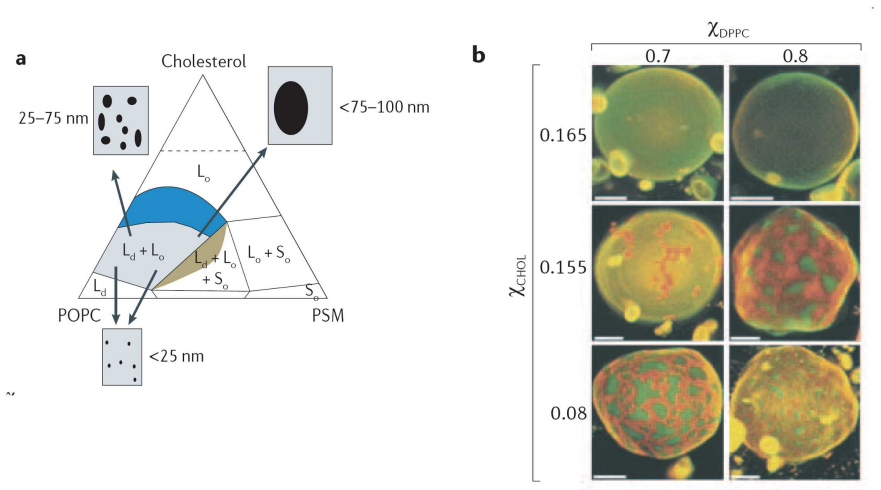

Figure 1.3: **Cholesterol Induced Partitioning on GUVS:** (a) The LO-LD phase diagram shows regions of Coexistence of the LO and LD phases (in blue). (b) Fluorescence images of GUVs labeled with dyes that preferentially partition into LO (orange) and LD (green) phases.

The mechanisms we have suggested so far are all *passive*: in the clathrin coated pit, we come across a situation wherein *proteins* recruit membrane molecules to create local heterogeneities ; in example II, the static actin cortex, thermally driven diffusion in the presence of actin corralls results in compartmentalization ; finally in example III, *lipid* heterogeneities drive compartmentalization.

1.1.4 A route to nano-scale compartmentalization

In Chapter 2 we describe the standardization of a non-invasive probe of lipid heterogeneities ([38][19]), which makes use of the phenomenon of Fluorescence Resonant Energy Transfer. The molecular probe used is the GPI-Anchored protein. This protein is

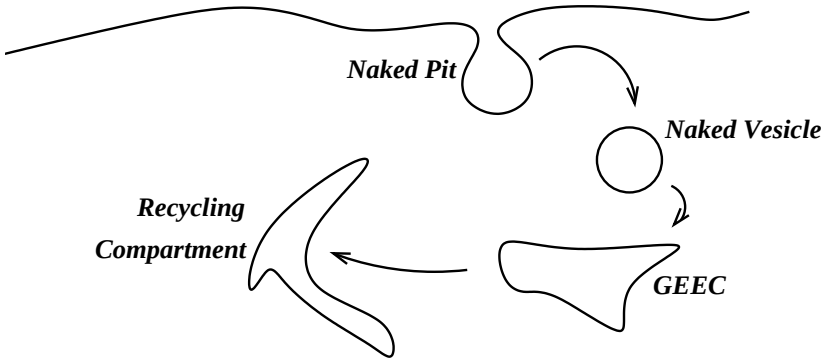

Figure 1.4: **GEEC Endocytosis.** Vesicles in this pathway find their way to the recycling compartment via the GEEC

attached to a saturated lipid anchor glycosylphosphatidyinositol (GPI) via an oligosaccharide backbone that binds to the C terminus of the protein, and is present on the upper (exoplasmic) leaflet of the plasma membrane. Many kinds of GPI-APs exist on the cell membrane, and they are functionally very varied. However, their lipid anchor dictates their behaviour on the membrane. In chapter 2, we summarize the results of Sharma et al, that suggest that the GPI-APs are organized in nanometer sized domains. The experiments discussed suggest that the formation and maintenance of heterogeneities of these molecules is an active process, highly dependent on the *dynamics* of the actin cytoskeleton.

GPI-APs are interesting functionally because they are endocytosed by a pathway which is independent of both clathrin and dynamin. Nascent endocytic vesicles enclosing GPI-APs form a compartment called GEEC (GPI-Enriched Endocytic compartment) [36]. Much of the fluid uptake of the cell is via this pathway. The GEEC pathway is unique in the following ways: (1) Unlike the clathrin mediated pathway, it does not need an external trigger like the binding of cargo and receptors and occurs even in the *absence* of GPI-APs.(2)The vesicle formed in this pathway have a range of sizes, unlike vesicles in the clathrin mediated pathway, whose radius is equal to the radius of the pit. The internalization of GPI-APs via this pathway is dependent on a specifically maintained organization of these proteins, characteristic of their lipid anchor. This pathway also crucially depends on actin machinery[13]. In chapter 2, we make attempts to characterize this organization.

Considerable evidence points to the existence of small, transient regions, enriched in cholesterol and sphingolipids, known in general as rafts. Proteins that attach on to the

plasma membrane with a saturated lipid tether, which have the capacity to associate with cholesterol in the way discussed above, are markers of these regions. Analysis of the single molecule tracks of CD59, one such molecule, by Kusumi et al [42], showed that a few of these (3-9) molecules undergo actin dependent temporary immobilization for about 0.57 seconds. Such entrapments was shown to cause further signaling into the cytosol. Thus these regions can act as signaling stations.

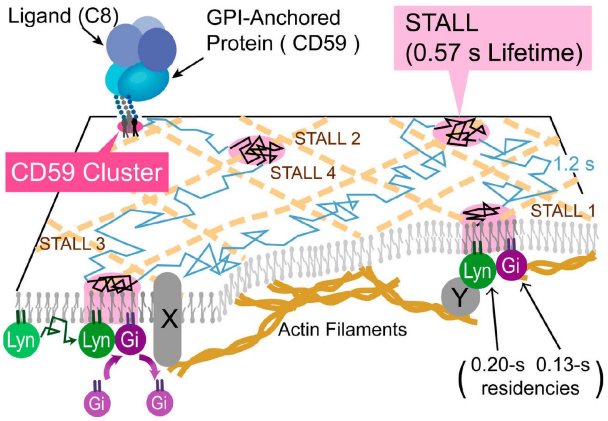

Figure 1.5: **The motion of CD59 on the membrane:** the motion of single particles of CD59 is stalled for 0.57 seconds, and upon entrapment, these molecules enhance the binding of molecules in the cytosol (Lyn and Gαi2), leading to further signaling events.(Courtesy [42])

We will see that the examples discussed previously are insufficient to explain the nanoscale organization of the plasma membrane, and we need to invoke the presence of the active actin cytoskeleton. The lipid matrix in which all membrane action takes place has an *actively* held apriori organization.

1.2 The Cell Cortex

1.2.1 Assembly of Actin

Actin is one of three members of the filaments making up the cytoskeleton, the others being microtubules and intermediate filaments. It is present in abundance just below the plasma membrane, and one its primary roles is to act as a scaffolding that imparts rigidity to the plasma membrane. It is a long stiff polymer, with individual monomeric

sub units arranging themselves in a helical manner. Actin subunits have a bound ATP molecule, whose hydrolysis is more probable when the subunit is part of the polymer. On hydrolysis, the subunit changes its configuration to one that is reactively asymmetric: it offers different binding sites on its two faces. This results in the actin filament having an overall polarity, and we can distinguish its 'plus' end from its 'minus' end. In its hydrolyzed form, a subunit can un-bind from a filament more easily, while ATP bound monomers can add on to the filament more easily.

The ATP hydrolysis step distinguishes actin from other polymers as the two ends of the filament have different polymerization and depolymerization rates because of this step. This results in the plus of the filament growing at a much faster rate than the minus end. An important consequence of this is treadmilling: local differences in monomer concentration at the two ends of a growing filament arise if the the two ends polymerize and polymerize at different rates. If the rates of polymerization(depolymerization) are $k_p^+(k_d^+)$ for the plus end of the filament, and $k_p^-(k_d^-)$ at the minus end, the local steady state monomer concentration at the two ends will be,

$$\begin{aligned} C_m^+ &= k_d^+/k_p^+ \\ C_m^- &= k_d^-/k_p^- \end{aligned}$$

By maintaining this difference in concentration, the filament is able to maintain a steady state length.

In the cell, actin polymerization is a controlled process involving nucleation, capping and decapping of actin monomers. The cell contains different types of nucleators of actin polymerization such as the ARP complex, formin proteins and spire, which can each result in different assemblies of actin [16]. The ARP complex for instance, nucleates actin by binding to one face of a subunit of the subunit, presenting the minus end for further polymerization. One binding site of the molecule sits on the side of a pre-existing filament, and another binds an actin monomer, thereby cross linking actin filaments at angles of roughly 70^o.

Monomers can be prevented from entering a filament by binding to a 'cap' (eg:thymosin) which prevent them from interacting with either the plus or minus end of a filament. Most of the monomeric actin in the cell is in this form, and decapping of actin occurs only when initiated by some other factor. The capping of monomers is affected by the presence of

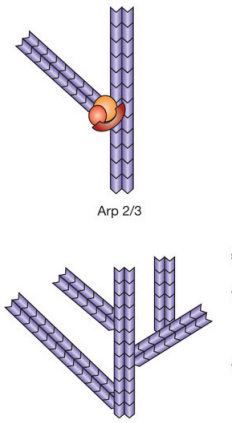

Figure 1.6: **ARP Activity**(Courtesy [16]): the ARP complex (in orange) binds to an existing actin filament (in blue), enabling cross linking of filaments, and initiating polymerization.

a third player, a protein (eg: profilin) that competes with the cap to bind to one face of the monomer, leaving the other face free to add on to a pre-existing filament. This competition between capping and inhibition of capping, sets the rate at which nucleated filaments grow.

1.2.2 Forces generated by actin

Polymerizing actin generates normal forces at a fluctuating surface. The mechanism of force generation has been understood in terms of the rectifying action of monomer addition [31]. As the surface thermally fluctuates, it is likely to create gaps between itself and the filament for a short time. In this short time, monomeric units can add on to the existing filament, thereby rectifying the motion of the surface.

Actin filaments also interact with the myosin family of motors, that transiently cross-link many actin filaments and affect their movement. Myosin II, one such motor, is a protein composed of two globular heavy chains (heads of myosin), and two light chains forming a coiled coil, as indicated in the figure 1.7. The heads of myosin can bind to two actin filaments, cross linking them, and hydrolyze ATP to walk from the minus end to the plus end of the filaments. The action of myosin gives a momentum to the bound parallel filament pair and makes an antiparallel pair of filaments slide with respect to one another in opposite directions. We discuss the consequences of actin-myosin interaction in greater detail in Chapter 4.

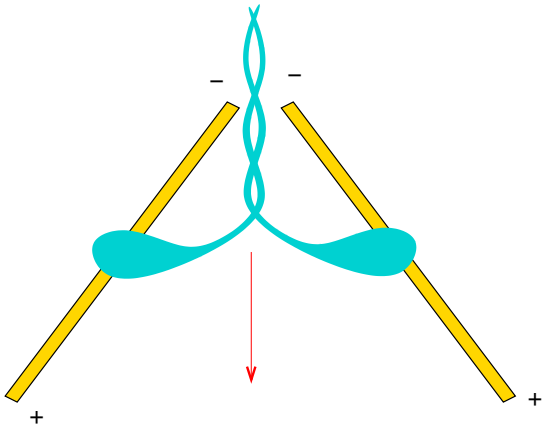

Figure 1.7: **A myosin motor** (in blue) walking on a pair of actin filaments

1.2.3 Actin near the membrane

Many molecular players exist that initiate actin polymerization *at* the cell membrane. Cdc42, a GTPase, is one such molecule. It is mostly present in its GDP-bound form in the cytosol. On activation, it brings about the polymerization of actin close to the membrane by recruiting the ARP complex. We will encounter this molecule in Chapter 3 as well, where we reason that it is one of the major players in recruiting actin that is predominantly vertically aligned with respect to the membrane. The recruitment of the polymerization machinery of actin to the surface is instrumental for cell locomotion and adhesion. The formation of cellular 'appendages' like lamellipodia, filipodia etc are triggered by the recruitment of the actin polymerizing machinery at the plasma membrane.

In the cell, actin has different arrangements according to the function that it serves. Most of the filaments in the 3D bulk of the cell form contractile bundles, serving as stress fibres (Figures 1.8 and 1.10) that adhere the cell to a substrate at focal points. Near the the plasma membrane, actin forms a cross linked 3D intermeshed shell, of about a micron in thickness. This shell in broken in parts to accommodate protrusive bundles of actin.

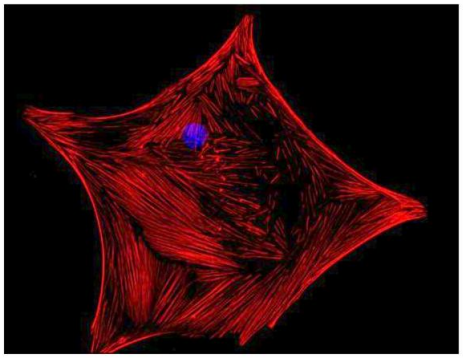

Figure 1.8: **Phalloidin stained F-Actin** (red) in a Mouse Leydig Cell, showing a large number of stress fibres and a rim of actin. (Courtesy www.img.cas.cz/dbc/gallery.htm)

There is considerable evidence to suggest that membranal appendages such as microvilli, filipodia, lamellipodia, ruffles etc contain protrusive bundles of polymerizing actin. [16]. The force exerted on the membrane by these bundles of actin is presumably a combination of both polymerization as well as myosin activity.

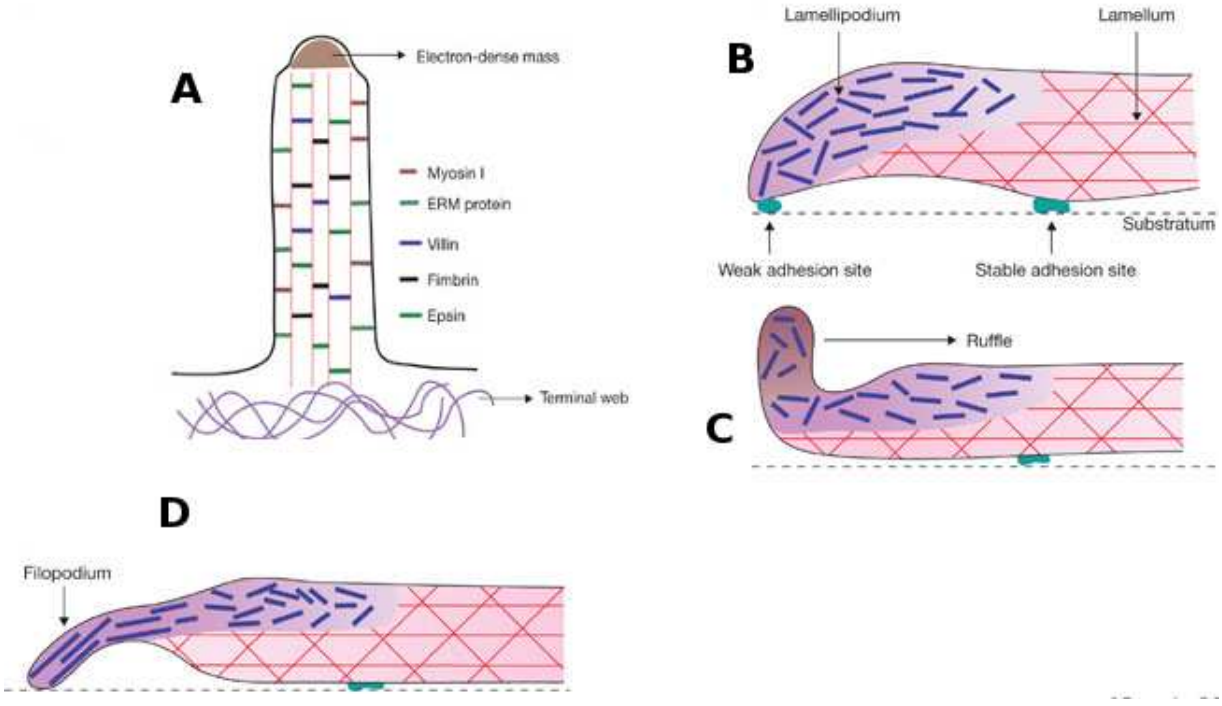

Figure 1.9: **Various Architectures of Actin** (Courtesy [16]): A. Microvilli containing vertical bundles of crosslinked actin. (B, C, D) Lamellipodia, ruffles and filipodia, containing polymerizing filaments that aid in locomotion.

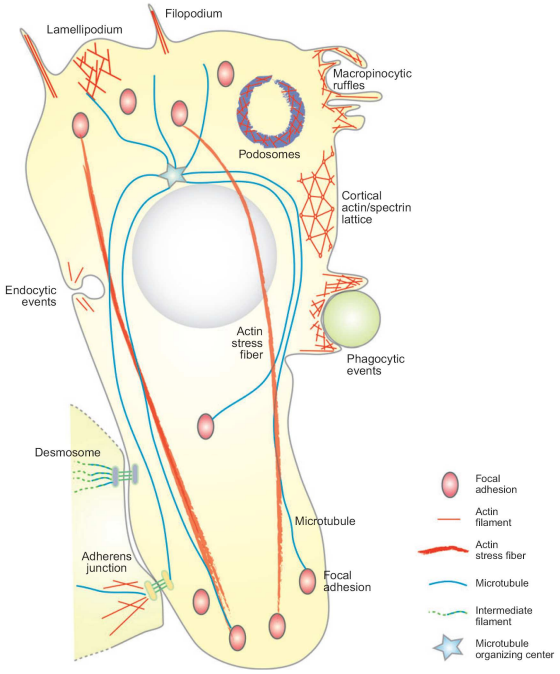

Figure 1.10: **Diverse array of actin architectures in the cell.** (Courtesy [17])

1.3 The Active Composite

With this general introduction to the actin meshwork and its properties, we can now go on to understand its effect on the plasma membrane. Both polymerization and myosin cross linking of actin make it a machine capable of generating forces. Hydrodynamic theories of acto-myosin suspensions view the actin-myosin complex as a force dipole due to this property, exerting active forces proportional to the orientation (the active stress is given by $\sigma_{ij} \sim p_i p_j$, $\mathbf{p}$ being the orientation) [40]. We have seen that actin is capable of directed force generation, which gives rise to shape changes. We now propose that such forces can also aid in molecular organization on the cell, by giving rise to directed *fluxes* of particles.

In chapter 2 we will describe a set of experiments probing the organization and dynamics of GPI-APs on the plasma membrane, and we conclude that this organization is highly dependent on the active forces exerted by a special architecture of cortical actin, organized tangentially (as opposed to vertically) with respect to the plasma membrane.

In chapter 3, we discuss the possible mechanisms by which cortical actin can change its architecture, thereby modulating its shape and composition.

Finally in chapter 4, we propose a coarse grained model of actively cross linked filaments, giving rise to directed fluxes at a surface. We suggest that these forces are responsible for the nanoscale organization of GPI-APs.

Chapter 2

Arrangement and Dynamics of GPI Anchored Proteins on the Cell Membrane

In this chapter, we describe non invasive means of probing GPI anchored proteins on the plasma membrane (PM). As mentioned in the introduction, the GPI-AP is a molecule that might be associated with cholesterol on the PM due to its lipid tail. The functions of GPI-APs themselves are varied: they act as cargo receptors in the GEEC pathway, and are responsible for the uptake of Folic acid [1]; they can act as activation antigens [30]in the immune system ; they act as strong apical targeting signals in polarized epithelial cells[24]. Besides this, the lipid anchors, and the ensuing cholesterol dependent organization, seem to confer on to GPI-APs much of their functionality. Disrupting the organization by cross linking these proteins obstructs their functions [29]. The maintenance of GPI-AP organization is therefore of appreciable importance. In section 2.1 and 2.2, we will summarize the fluorescence spectroscopy techniques used and results previously obtained by our lab [38], that suggest that the GPI-APs live as monomers or nanoclusters on the plasma membrane. In later sections, we will describe the use of a variety of fluorescence techniques in furnishing information about the steady state spatial distribution and steady state dynamics of GPI-APs.

2.1 Previously, on GPI-APS

Heterogeneities in GPI-AP organization are not seen in an optical microscope, as discussed in the first chapter, and they are suspected to live as nanometer sized domains. In order to "see" these domains, fluorescence microscopy is thus insufficient. In an earlier study by our lab, the signal from Fluorescence Resonant Energy Transfer (FRET), a phenomenon very sensitive to intermolecular distances, was used to probe GPI-AP architecture. In this section we discuss this technique and its use in probing molecular architecture, and summarize the results of earlier FRET measurements.

2.1.1 FRET and Polarization Anisotropy

A fluorophore in solution, excited by polarized light, can take the following routes to ground state:

(a) **It can spontaneously emit a photon**. This is the well known phenomenon of fluorescence: the excited fluorophore moves to ground state via an initial non-radiative decay to a lower vibrational level, and consequently, the emission of a photon. The emitted photon is red shifted with respect to the incident photon.

Fluorophores absorb and emit radiation of polarization parallel to their transition dipole moments. Absorption is maximum when the dipole moment is parallel to the incident polarization $\vec{P}_I$, however, due to rotational diffusion, the emitted light is usually not parallel to $\vec{P}_I$.

Emitted photons from a very dilute solution of fluorophores can be collected with two polarizers parallel (yielding an intensity $I_{||\infty}$) and perpendicular (intensity $I_{\perp\infty}$) to $\vec{P}_I$. $I_{||\infty}$ and $I_{\perp\infty}$ will have a non zero difference, called the anisotropy at "infinite dilution", and this quantity serves as a measure of depolarization due to rotational diffusion.

$$A_\infty = \frac{I_{||\infty} - I_{\perp\infty}}{I_{||\infty} + 2I_{\perp\infty}}$$

(b) **It can pass on the energy to a neighbouring fluorophore, which then spontaneously emits a photon**: Forster showed that when an excited fluorophore (a donor) has a neighbour (an acceptor) in the ground state, it can transfer all its energy to the

neighbour, provided their separation is less than a critical distance. This phenomenon is known as Fluorescence Resonant Energy Transfer (FRET). It occurs due to induced dipole-dipole interactions between the transition dipoles of the donor and acceptor. According to Forster's theory[5], the efficiency of FRET is a function of the distance R between the donor and the acceptor

$$E = \frac{1}{1 + (R/R_0)^6}$$

R_0, the Forster's radius, is a parameter that incorporates the spectral overlap between the donor and acceptor as well as the orientational correlations between the two. After transfer, the acceptor, which need not be aligned with the donor, then emits a photon to return to the ground state.

In an experiment, we can choose the donor and acceptor to be two different kinds of molecules (Hetero-FRET). The excitation spectra of the two may be well separated, but the emission spectrum of one should have a finite overlap with the excitation spectrum of the other. The frequency of the emitted lighted is then a marker of FRET activity, and its intensity tells us about the proportion of FRET events. The donor and acceptor can be chosen to be identical (Homo-FRET), but their orientations need not be the same. The acceptor therefore emits a photon depolarized with respect to $\vec{P_I}$. This is then measured as an anisotropy, defined by

$$A = \frac{I_{||} - I_{\perp}}{I_{||} + 2I_{\perp}}$$

(c)**It can interact with the medium**, which quenches its fluorescence: Dissipation of the energy into the medium via collisions, and chemical reactions of the fluorophore with the medium, can both quench the fluorophore. The excitation light can also photobleach fluorophores, by creating free radicals in the medium, that consequently quench fluorescence. Photobleaching is an externally tunable parameter, that can be made use of in an experiment to derive information, as we shall see later.

2.1.2 A summary of known results

In order to probe the organization of GPI-APs on the cell membrane, Sharma et al[38] conducted a nested set of FRET measurements on fluorescently tagged GPI-APs. The intention was to look for rafts, the hypothesized lipid heterogeneities described in Chapter 1, and FRET being a direct indicator of density variations, was the natural choice as probe. The fluorescent tags chosen for the experiments are GFP and PLF. The GFP tag encloses the parent molecule, and PLF is attached to it parent molecule via a hinge. Both these tags allow the GPI-APs to rotate in the ambient medium.

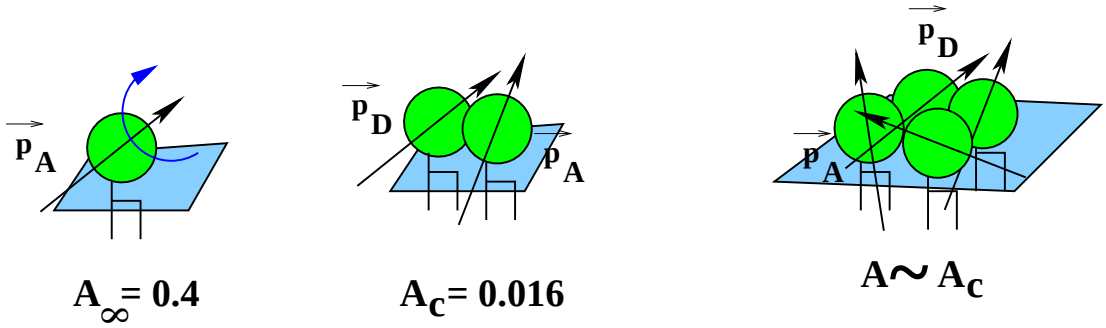

Figure 2.1: **Anisotropy values of different configurations** (A) A freely rotating isolated fluorophore (B) A pair of fluorophores close enough for FRET (C) A group of fluorophores within a Forster's radius of each other.

One can calculate anisotropy values of simple configurations of these labeled proteins on a membrane, by assuming that the fluorophores are uniformly oriented on a unit sphere (Figure 2.1). Depolarization due to FRET yields an anisotropy value (A_c = 0.016) considerably less than A_∞. A very low anisotropy is therefore reflective of a dense distribution of fluorophores. Increasing the number of fluorophores within the Forster's radius does not change the value of anisotropy much [8], the anisotropy of a dense cluster with three fluorophores will almost be equal to A_c.

Whole cell polarization anisotropy measurements yielded a roughly constant value over a range of expression levels. Indeed, the value was low compared to A_∞ even for low expressions of the protein, indicating a highly inhomogeneous clustered environment.

Paradoxically, the signal from Hetero-FRET was very weak, almost reaching the levels of noise.

To resolve this, they proposed a model of organization (model C in Figure 2.2) where a large fraction of clusters of GPI-APs, of coordination number of not more than 4-5 per cluster, live in a monomer pool. These clusters are dense, with an interparticle separation less than a Forster's radius (4.7 nm for PLF). Different GPI-APs occupy the same cluster, and there is a free exchange of material between the clusters and the pool. The energy required to form a cluster is very low, much lower than typical covalent binding energies ($10k_BT$). The features of this model were contrasted with that of (A) where a dense patch of GPI-AP's is separated from a pool of dilute monomers and (B) a variant of C, where proteins are organized at the boundary of the domain.

Model C is backed up experimentally by two key results:

1. Bleaching of similarly labeled fluorophores on the cell membrane, can be used to dilute the fluorescence from the clustered regions. While model A would require sufficient dilution to have taken place before the anisotropy changes, model C accounts for a *rapid* change in anisotropy on dilution, which is what is seen in the experiments.

2. Two kinds of GPI-APs (A and B) are co-expressed on the membrane. When A is crosslinked with an antibody, one notices that B reorganizes to form clusters while A is completely crosslinked. Clusters therefore contain different kinds of GPI-APs, and can exchange their constituents with both the monomer bath and other clusters. The energy keeping molecules together has an upper bound, given by the covalent binding energy of A and the antibody.

Model C explains the lack of Hetero-FRET signal, as the probability of having different fluorophores in the same cluster is low for a low coordination number. The coordination number is predominantly 2, but not more than 4. Independent experiments show that about 20-40 % of the population of GPI-APs live in clusters.

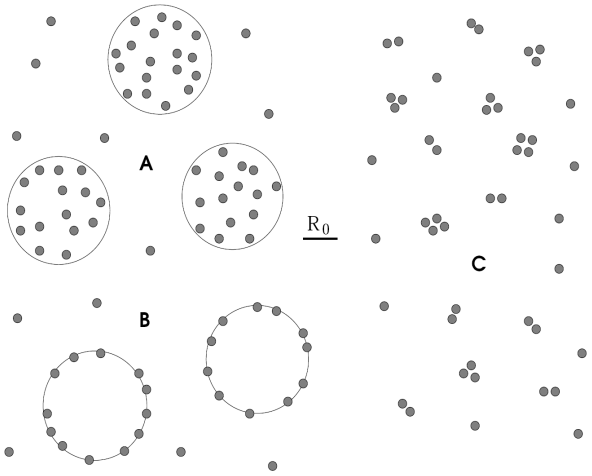

Figure 2.2: **Possible Models for the Organization of GPI-APs on the cell membrane.** Model C conforms with the results of detailed modelling [38]. R_0 is the Forster's radius. (Courtesy Sarasij R C ; PhD thesis ; 2004)

2.1.3 Aim of the experiments

Model C highlights the interesting non-equilibrium origin of the cluster. Consider, for illustration, the dimerization of two monomers. The law of mass action requires that the ratio of the concentrations of dimers (x_2) and monomers (x_1) be related by stoichiometry: $x_2 \propto x_1^2$. However, as mentioned earlier, this ratio is *constant* over a large range of expression levels (a measure of the total number of fluorophores). Violations of mass action can arise due to large spatial variations in concentrations, or due to the nature of cluster formation itself [29]. The experiments presented in this chapter aim to probe both spatial variations, as well as local dynamics of clusters and monomers, leading to an understanding of formation, and maintenance of GPI-AP architecture.

2.2 Spatial distribution

2.2.1 Large Scale Features

Wide field and confocal imaging (with a spatial resolution of $300 \times 300nm^2$) of fluorescently labeled GPI-APs gives us a bird's eye view of the anisotropy landscape on the cell membrane[19]. Maps of Anisotropy (A) and Intensity (I) reveal large variations over the

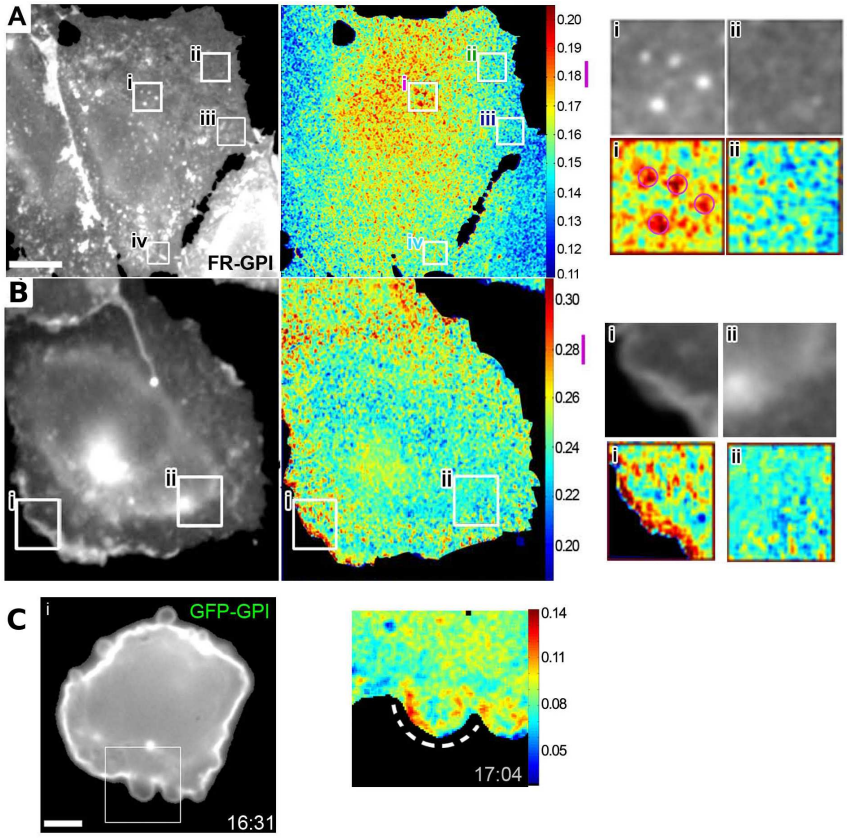

Figure 2.3: **Large scale variations in anisotropy.** A and B are plated CHO (Chinese Hamster Ovary) cells whose surface is labeled with fluorescently tagged FR-GPI (PLF labeled folate receptor) at 20^oC. C is a snapshot of a freshly adhering fibrobast sprouting blebs as its actin meshwork re-organizes. A (i), B(i) and C(i) are microvilli, ruffles and blebs respectively, all with no nanoclusters. The flat regions A (ii) and B(ii) are rich in nanoclusters.

scale of $\sim 450nm$. Highly polarized regions (with very few nanoclusters), are associated with membrane protrusions like microvilli (Figure 2.3 A(i)), lamellipodia, ruffles (Figure 2.3 B (i)) etc. In contrast, the vast 'flat' landscape (Figs 2.3 A(ii), 2.3 B(ii)), the flat lamellum preceding the lamellipodia (Fig 2.3 A (iii)), are both low in anisotropy. Recall the distinct actin architectures of these structures - while in the first set of structures, the actin points towards the membrane, in the second, it is mostly parallel to the membrane. Spontaneously forming blebs in cells in the process of adhering to a substrate, known to be devoid of actin, are devoid of clusters as well (Figure 2.3 C).

2.2.2 Anisotropy distributions of 'typical' regions of the membrane.

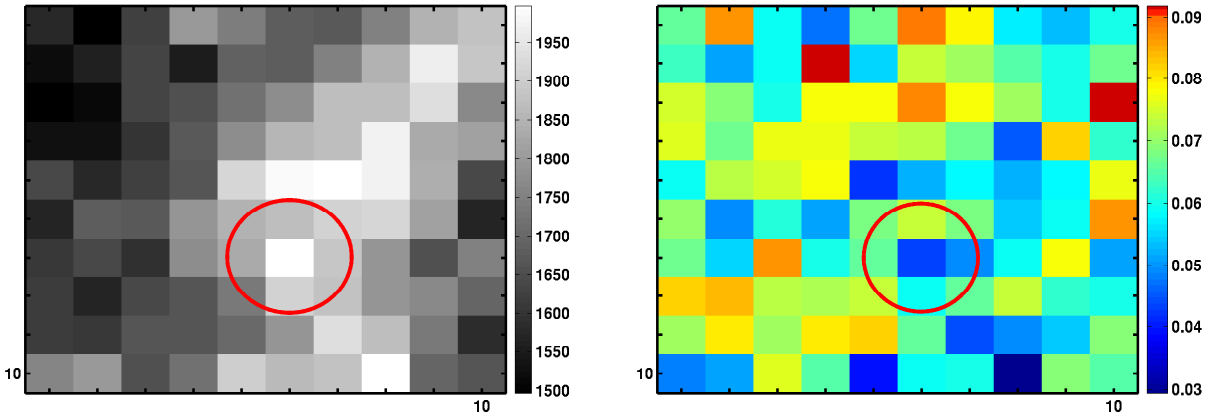

Figure 2.4: A 10×10 (300 nms per pixel) patch of membrane showing (a) Intensity and (a) anisotropy. The encircled pixel has flanks in the intensity map but not in the anisotropy map.

In addition to the large scale differences in anisotropy values, 'typical' patches of featureless membrane (Figure 2.3 A (ii), Figure 2.5 A(i,i')) also contain valuable information. The images are collected over a time window of one second, with a rate of one frame per second. Before any analysis of the image is done, the images have to be cleaned. We are interested in steady state features of the anisotropy distribution, and therefore first remove all high frequency information by averaging over a few consecutive frames (5).

The image has to be spatially cleaned as well. Any image acquisition blurs the true image via a point spread function (P_I), which in our case has a width of 3 pixels. A fluorescent

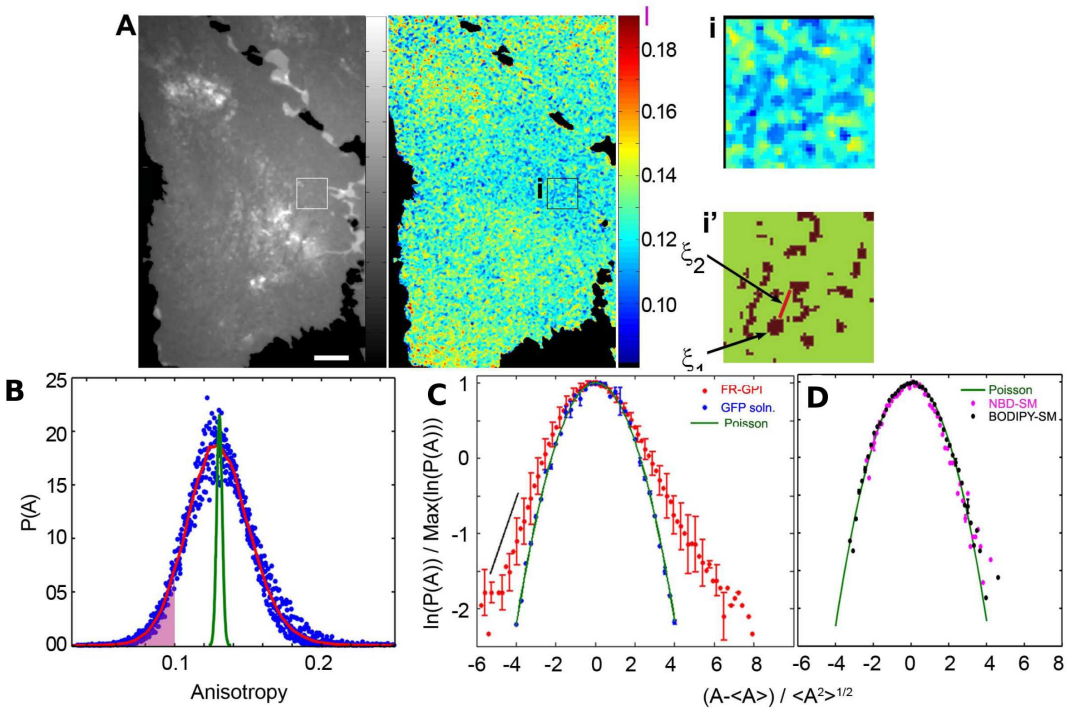

Figure 2.5: **Typical features of a cell.** (A) The depolarized pixels, with anisotropy values less than a threshold = 0.1 (the pink shaded region in 2.5 B) form 'islets' of characteristic size ξ_1 and separation ξ_2 (A i'). (B) A typical distribution can be ascribed to the control cells (red curve), which is considerably broader than a Poisson distribution of clusters and monomers (green curve). (C) The typical distribution has exponential tails as opposed to the Poisson distribution and a solution of GFP molecules. (D) Bulk membrane markers, such as short chained lipids (Sphingomyelin labeled with fluorescent dyes NBD and BODIPY), in contrast, do not have exponential tails and coincide with the Poisson distribution.

molecule therefore can be detected anywhere in box of 3×3 pixels surrounding it, with a probability showing a Gaussian decay from the central pixel. To get a true representation of intensity, one would have to deconvolve this map and remove the effect of the point spread function. However, an anisotropy signal is detected, when two fluorophores are simultaneously present in the same pixel. For a cluster of coordination number 'n', this means that the probability of detection P_A is the product of the n point spread functions of the constituent monomers. Compared to P_I, P_A has hardly any weightage in the flanks surrounding the central pixel. The time averaged image of intensity shows bright pixels always surrounded by flanks of lesser intensity (Figure 2.4 a). The corresponding time averaged anisotropy map (Figure 2.4 b) on the other hand contains isolated pixels of either high or low anisotropy, each pixel reporting the true anisotropy in the region.

No spatial deconvolution of the anisotropy map is necessary, and we go on to plot a distribution of the single pixel anisotropy values.

Our sample data consists of flat regions of the cell membrane, of not more than 50×50 pixels in area. The intensity due to monomers $\langle I_m \rangle$ and clusters $\langle I_c \rangle$ can be separately calculated using the average intensity $\langle I \rangle$ and anisotropy $\langle A \rangle$ of the patch.

$$\begin{aligned} \langle I_m \rangle &= \frac{(\langle A \rangle - A_c)\langle I \rangle}{A_m - A_c} \\ \langle I_c \rangle &= \frac{(\langle A \rangle - A_c)\langle I \rangle}{A_c - A_m} \end{aligned}$$

where we have taken $A_m = 0.18$ and $A_c = 0.04$ [38]. If we randomly scatter clusters and monomers on the patch, the anisotropy distribution will be a combination of two independent Poisson distributed intensities with means $\langle I_c \rangle$ and $\langle I_m \rangle$ respectively. We generate strings $\{I_m\}, \{I_c\}$of intensity values by drawing random numbers from Poisson distributions with these means, to obtain a string of anisotropy values

$$\{A\} = \frac{A_m\{I_m\} + A_c\{I_c\}}{\{I_m\} + \{I_c\}}$$

The distribution of $\{A\}$ can then be compared with observations.

The normalized distributions of cells' anisotropy fall roughly on top of each other for different patches, for different cells, which allows us to ascribe a typical distribution of anisotropy to a cell (The red curve in Figure 2.5 B). There are a very large number of pixels lying outside the limits of the generated Poisson distribution (The green curve in Figure 2.5 B). The typical distribution has *exponential* tails, as opposed to the Gaussian tails of the Poisson distribution, on either side of the mean anisotropy (Fig 2.5 C). As negative controls, the anisotropy distributions of bulk membrane markers like Sphingomyelin labeled with fluorescent dyes NBD and BODIPY, were found to have Gaussian tails (Figure 2.5 D). There is therefore, a larger weightage in the tails of the distribution, than is allowed by free mixing of clusters and monomers. This study proves that there exist regions on the membrane, less than $300nm^2$ in area, with both very large and very small number of clusters, even in the flat regions.

The proportion of pixels with anisotropy values less than an arbitrary cutoff (0.1) defines for us a parameter ϕ, marked by the pink shaded region in Figure 2.5 (B), which is useful when we study perturbations of cholesterol and actin (Section 2.5).We find that the highly depolarized regions, with anisotropy values less than the cutoff are found as 'islets' (Figure 2.5 (A)), isolated and disconnected patches on the membrane, with a typical size $\xi_1 \leq 450nm$ and a typical separation ξ_2 of order $800 - 1250nm$. A uniform distribution of the islets in the sample area would lead to a separation of about $3000nm$, suggesting that these domains are in turn further clustered, giving rise to a distinct hierarchical distribution of the nanoscale clustering.

2.3 Steady State Dynamics

2.3.1 Bleaching as a probe of dynamics

The steady state anisotropy and intensity $(A(t), I(t))$ of a small region of the membrane measured under ideal conditions (no bleaching), typically would fluctuate about an average value. We would like to know what the processes leading to the steady state are, their rates and relative contributions, without disturbing the architecture of the membrane. In a test tube reaction, it is possible to control the initial concentrations of the reactants, the onset of the reaction, and monitor product concentrations as time progresses. On the cell membrane, local concentrations cannot be tampered with. Photobleaching the cell membrane, can dilute the system to create a desired initial condition by destroying fluorescence, a fact which is routinely made use of in techniques like FRAP (Fluorescence Recovery After Photobleaching).

The experiment described here uses the incident light to excite, as well as photobleach fluorophores in a small confocal spot enclosing a part of the membrane. The signal is recorded in two illuminations $0 < t < t_1$ and $t_1 + t_w < t < t_2$ separated by a waiting time t_w(during which the laser is switched off). During the first illumination period, $I(t)$ shows a rapid decay followed by a slower decay to a low value. It partially recovers during the waiting period, after which it starts decaying again. The corresponding $A(t)$ trace, broadly shows two different kinds of behaviour that significantly correlate with temperature. At 20^oC, $A(t)$ typically starts out at a low values reflective of a significant cluster concentration, and shows a sharp initial rise before saturating to the anisotropy value at infinite dilution A_∞. After the waiting time, the anisotropy value recovers

negligibly although the intensity has considerably recovered. In sharp contrast, at 37^oC, a low initial value of A, saturates to a value much lower than A_∞ and after the waiting time, almost completely recovers its original value.

At 20^oC, clusters are neither being formed, nor do they diffuse in from surrounding regions, as seen by the lack of anisotropy recovery. This could either happen if the clusters either are not present in surrounding regions or if they are immobilized. It is possible to ascertain the cause by simultaneously monitoring the anisotropy of a central patch, where bleaching takes place, and two surrounding patches that could act as reservoirs of clusters and monomers. A photostable analogue of Folic acid (PLB) is used for this purpose, in order to minimize the effect of bleaching in the surrounding regions. The central region (pink box in Figure 2.6 C,E), with a low initial anisotropy, is then bleached, and as is expected, the anisotropy value does not recover post bleaching. One would expect the effects of cluster diffusion to show up after waiting for 4 minutes post bleaching, however, very little recovery is detected. The surrounding pixels (blue and brown box in Figure 2.6 C,E) are not bleached, and their anisotropy values remain roughly the same throughout the experiment. One can conclude therefore, that the surrounding regions *do not* act as a reservoir of clusters for the central bleached regions. This experiment (called ARAP: Anisotropy Recovery After Photobleaching) acts as an independent check of the immobilization of clusters.

However at 37^oC, clusters are constantly present in the face of bleaching, indicating that there is a constant conversion of monomers into clusters. The recovery of anisotropy after the waiting time is again indicative of formation of clusters, however it could also mean that there is significant cluster diffusion at this temperature. An ARAP experiment confirms once more that diffusion is not the cause of recovery: notice in particular that during bleaching, the anisotropy of the surrounding regions are significant *lower* than their starting values. Clearly monomers are being lost from these regions, but not clusters.

Chemical equilibrium requires that the formation of clusters be balanced by the fragmentation of clusters. All the kinetic features mentioned in this section are now put together in a chemical kinetics model which we finally use to extract rates.

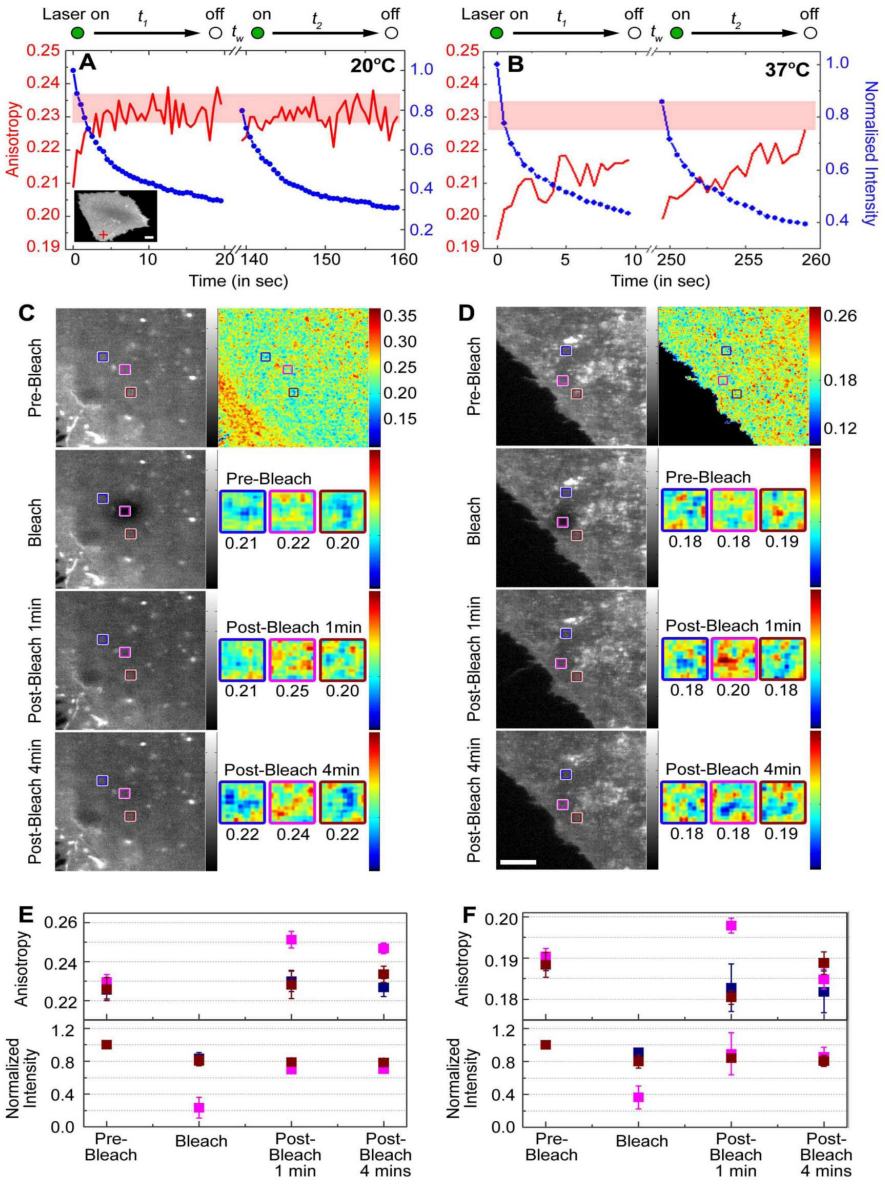

Figure 2.6: **Bleaching a small confocal spot on the membrane.** A and B are typical traces of anisotropy and intensity during the two bleaching periods $0 \leq t \leq t_1$ and $t_1+t_w \leq t \leq t_2$ for the temperatures 20^oC and 37^oC. While in A, recovery of anisotropy is almost absent post bleaching, in B, we see a considerable amount of anisotropy recovery. In C and D, three regions are monitored at 20^oC and 37^oC. The central region (in pink) is bleached. The anisotropy in surrounding regions (blue and brown boxes) is almost the same as the central region, and does not increase in time (E and F -20^oC and 37^oC respectively) during the bleaching of the central region at both temperatures, indicating that these regions do not replenish the central region's nanoclusters via diffusion. At 20 ^oC, the anisotropy in the pink box does not recover even after 4 minutes post bleaching.

2.3.2 Extracting parameters

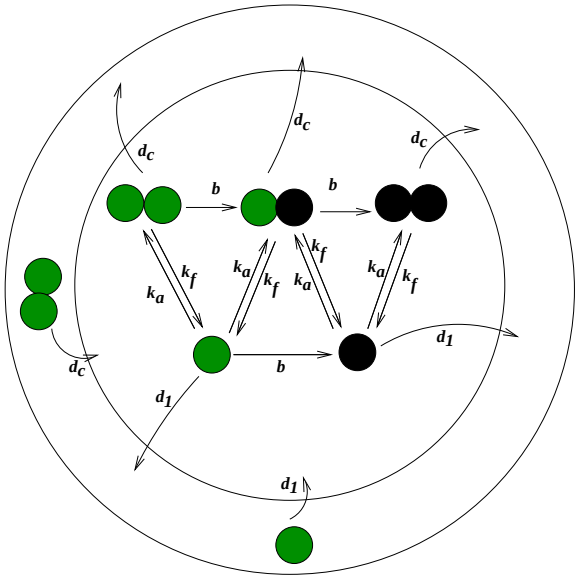

Figure 2.7: **A schematic model of monomer-dimer dynamics.** Active fluorophores (green) present in a confocal volume (inner circle) are bleached (black) independent of whether they are in a dimer or a monomer. Monomers and dimers interconvert with rates k_a and k_f respectively. They diffuse out of the confocal volume with rates d_1 and d_c, are a replenished from the pool outside (the annulus outside the confocal volume) with the same rates.

Figure 2.7 is a schematic of an illuminated plane of area V and perimeter p, showing diffusion and interconversion of clusters (dimers in the figure) and monomers in a confocal volume. In a time interval dt, every fluorophore bleaches with a probability b, whether or not it is part of a cluster. A cluster(monomer) can move in and out of the confocal volume with a probability $d_c dt(d_m dt)$. Most importantly, a cluster can fragment at a rate $k_f dt$, and monomers can cluster together at a rate $k_a dt$. Let c_{nm} be the concentration of clusters of coordination number n, with m active fluorophores. For a local description of dynamics, the way to proceed is to write down a system of reaction diffusion equations for all the species in a small volume dA. We restrict ourselves to a mixture of dimers and monomers, and arrive at the following equations

$$
\begin{aligned}
\partial_t c_{22} &= D_c \nabla^2 c_{22} - 2b c_{22} - k_f c_{22} + \frac{k_a dA c_{11}^2}{2} \\
\partial_t c_{21} &= D_c \nabla^2 c_{21} - b c_{21} + 2b c_{22} - k_f c_{21} + k_a dA c_{11} c_{10} \\
\partial_t c_{20} &= D_c \nabla^2 c_{20} + b c_{21} - k_f c_{20} + \frac{k_a dA c_{10}^2}{2} \\
\partial_t c_{11} &= D_1 \nabla^2 c_{11} - b c_{11} - k_a dA c_{11}^2 - k_a v dA c c_{10} + 2k_f c_{22} + k_f c_{21} \\
\partial_t c_{10} &= D_1 \nabla^2 c_{10} + b c_{11} - k_a dA c_{10}^2 - k_a dA c_{11} c_{10} + 2k_f c_{20} + k_f c_{21}
\end{aligned}
$$

We define an integrated quantity $C_{nm} = \int dA c_{nm}/N$, the fraction of n-mers, m of which are unbleached, within the confocal area. N here is the initial number of fluorophores contained in the area. The quadratic terms are decoupled using a mean field approximation.

$$
\int c_{nm} c_{n'm'} dA dA' = \int c_{nm} dA \int c_{n'm'} dA' = C_{nm} C_{n'm'} N^2
$$

The diffusive flux cancels out within the confocal volume and integrates to a surface term

$$
\int \nabla^2 c_{nm} dA = \oint \nabla c_{nm} \cdot \mathbf{dl} = N(C_{nm}|_{R^+} - C_{nm}) \frac{D_n p}{aV}
$$

Here the suffix $|_{R^+}$refers to the concentration just outside the confocal volume. 'a' is the thickness of the boundary circle, corresponding to the decay length of the intensity of illumination in the plane of the surrounding membrane. We assume that the bath is initially identical to the confocal spot: $C_{nm}|_{R^+}$ is given by the value of C_{nm} inside the confocal volume at $t = 0$, and does not change with time. We finally have ODE's for the C_{nm}s,

$$
\begin{aligned}
\frac{dC_{22}}{dt} &= d_c(C_{22}(0) - C_{22}) - 2bC_{22} - k_f C_{22} + \frac{k_a N C_{11}^2}{2} \\
\frac{dC_{21}}{dt} &= d_c(C_{21}(0) - C_{21}) - bC_{21} + 2bC_{22} - k_f C_{21} + k_a N C_{11} C_{10} \\
\frac{dC_{20}}{dt} &= d_c(C_{20}(0) - C_{20}) + bC_{21} - k_f C_{20} + \frac{k_a N C_{10}^2}{2} \\
\frac{dC_{11}}{dt} &= d_1(C_{11}(0) - C_{11}) - bC_{11} - k_a N C_{11}^2 - k_a N C_{11} C_{10} + 2k_f C_{22} + k_f C_{21} \\
\frac{dC_{10}}{dt} &= d_1(C_{10}(0) - C_{10}) + bC_{11} - k_a N C_{10}^2 - k_a N C_{11} C_{10} + 2k_f C_{20} + k_f C_{21}
\end{aligned}
$$

The initial conditions are provided by the experiment's starting values of A and I.

$$
\begin{aligned}
C_{22}(0) &= \frac{(A(0) - A_m)}{2(A_c - A_m)} \\
C_{11}(0) &= \frac{A(0) - A_c}{A_m - A_c}
\end{aligned}
$$

Unbleached species are not present at the start of the experiment. Therefore $C_{21}(0) = C_{20}(0) = C_{10}(0)$. A simplifying assumption reduces the number of equations to 3 and casts them in a linear form. We assume, that bleaching does not change the sum $C_{11}(t)+C_{10}(t)$. This means that the total number of bleached and unbleached monomers, at steady state, remains statistically constant. Finally, we see that the fractional intensities coming from clusters and monomers, $C_2 = 2C_{22} + C_{21}$and $C_1 = C_{11}$obey linear ODE's.

$$
\begin{aligned}
d_t C_2 &= -2bC_2 - k_f C_2 + k_a C_1 C_1(0) + d_c(C_2(0) - C_2) \\
d_t C_1 &= -bC_1 - k_a C_1 C_1(0) + k_f C_2 + d_1(C_1(0) - C_1)
\end{aligned}
$$

These two equations provide for us the normalized intensity trace $i(t) = I(t)/I(0) = C_2(t) + C_1(t)$. The anisotropy trace requires us to solve for an additional variable $C_{22}(t)$, to give $A(t) = (A_c C_{22}(t) + A_m(C_2(t) - 2C_{22}(t) + C_{11}(t)))/(C_2 + C_1)$.

Our reduction of the kinetic processes to a linear system of ODE's casts the solutions in the following form:

$$
\begin{aligned}
C_1(t) &= C_1(\infty) + B_{11}e^{-r_1 t} + B_{12}e^{-r_2 t} \\
C_2(t) &= C_2(\infty) + B_{21}e^{-r_1 t} + B_{22}e^{-r_2 t} \\
C_{22}(t) &= C_{22}(\infty) + B_{31}e^{-r_1 t} + B_{32}e^{-r_2 t} + B_{33}e^{-r_3 t}
\end{aligned}
$$

For the intensity, it clearly implies two routes of decay: the first with a rate $r_1 \sim 2b + d_c + k_f$, or the effective rate of loss of a cluster, the second with a rate $r_1 \sim b + d_1 + k_a C_1(0)$, the effective rate of loss of monomers. The steady state values $\{C_1(\infty), C_2(\infty), C_3(\infty)\}$, amplitudes $\{B_{11}, B_{12}, B_{21}, B_{22}, B_{31}, B_{32}, B_{33}\}$ and rates $\{r_1, r_2, r_3\}$ are all functions of the bare kinetic parameters $\{d_1, d_c, b, k_f, k_a, C_2(0), C_{22}(0), C_1(0)\}$ and a simple fit procedure is used to find them. The procedure keeps in mind the following points:

1. The two illuminations are representative of the same patch of membrane, and hence should have the same steady state values $\{C_1(\infty), C_2(\infty), C_{22}(\infty)\}$, and rates $\{r_1, r_2, r_3\}$, but the amplitudes $\{B_{11}, B_{12}, B_{21}, B_{22}, B_{31}, B_{32}, B_{33}\}$, a measure of relative weights of cluster and monomer signals, can vary.

2. The steady state values that can be obtained from the fit are $i(\infty) = C_1(\infty) + C_2(\infty)$, and $A(\infty) = (A_m C_1(\infty) + A_m(C_2(\infty) - C_{22}(\infty)) + A_c C_2(\infty))/i(\infty)$. The other parameters obtained from the fit of the intensity traces are $\{r_1, r_2, B_{11}, B_{12}, B_{21}, B_{22}\}$. From these, the bare parameters can be found, using expressions listed in the appendix at the end of this chapter.

2.3.3 Results of modelling

We fit the (A,I) traces and solve for $\{d_1, d_c, k_f, k_a\}$ for a set of temperatures $T \epsilon \{15^o C, 20^o C, 24^o C, 28^o C, 33^o C, 37^o C\}$. The diffusion rates of a cluster d_c obtained from the fits are always small compared to the other rates, lying within the interval $(-10^{-5}, 10^{-5})$. It is useful to set this value to zero to obtain better fit parameters (Fig 2.8 and 2.11). We find that the rates k_a and k_f have a large variability (Fig 2.8) at each temperature, but find themselves predominantly in one of four classes: No-Interconversion (NI), No Recovery (NR), Partial Recovery (PR) and Full Recovery (FR). Figure 2.9 contains representative traces, fits and parameter values for each of these classes. Typical values of k_a and k_f are picked from the dominant class in each temperature (marked

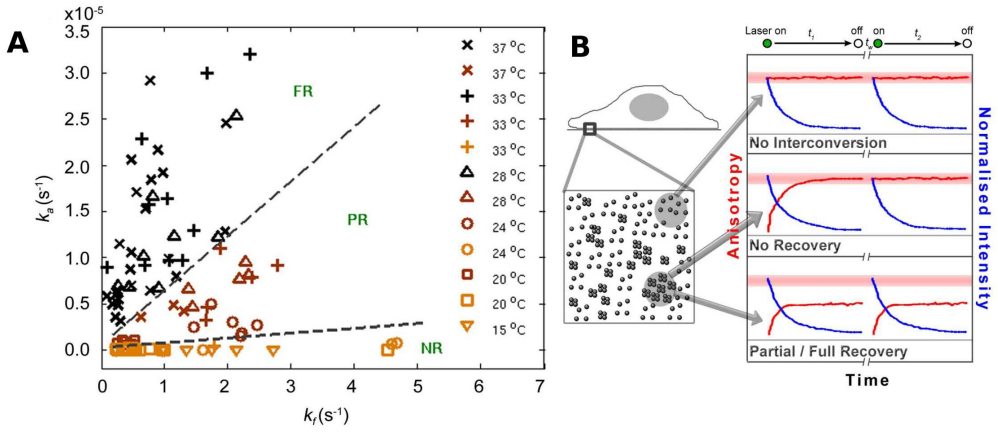

Figure 2.8: **Fit Parameters k_a and k_f.** (A) Aggregation rates k_a and fragmentation rates k_f found from the fits, fall into three broad categories: Full Recovery (FR), Partial Recovery (PR) and No recovery (NR). (B) An additional class (No interconversion, NI) can also be identified, where initially no nanoclusters are contained in the confocal volume. The three panels represent typical time traces belonging to the classes NI, NR and PR/FR.

with red in Figure 2.10 A), and are used to plot $log(k_a/k_f)$ against $1/T$, known as the 'Arrhenius' plot (Figure 2.10 B). Dimerization of monomers through a covalent bond formation will yield a linear Arrhenius plot, with a slope of $-\Delta E/k_B$, ΔE being the energy required for dimer formation. However, we obtain a very non-linear Arrhenius curve where ratio of the rates changes sharply above 24^oC. One can extract a typical value for $\Delta E/k_BT \sim 10^{-2}$ from the slope of the curve above 24^oC. This reflects the binding energy of nanoclusters [4]; this is 2–3 orders of magnitude lower than the minimal (van der Waals) interactions between molecules on a membrane at a similar intermolecular distance, and the antibody-binding energy ($\sim 10k_BT$) mentioned in subsection 2.1.2.

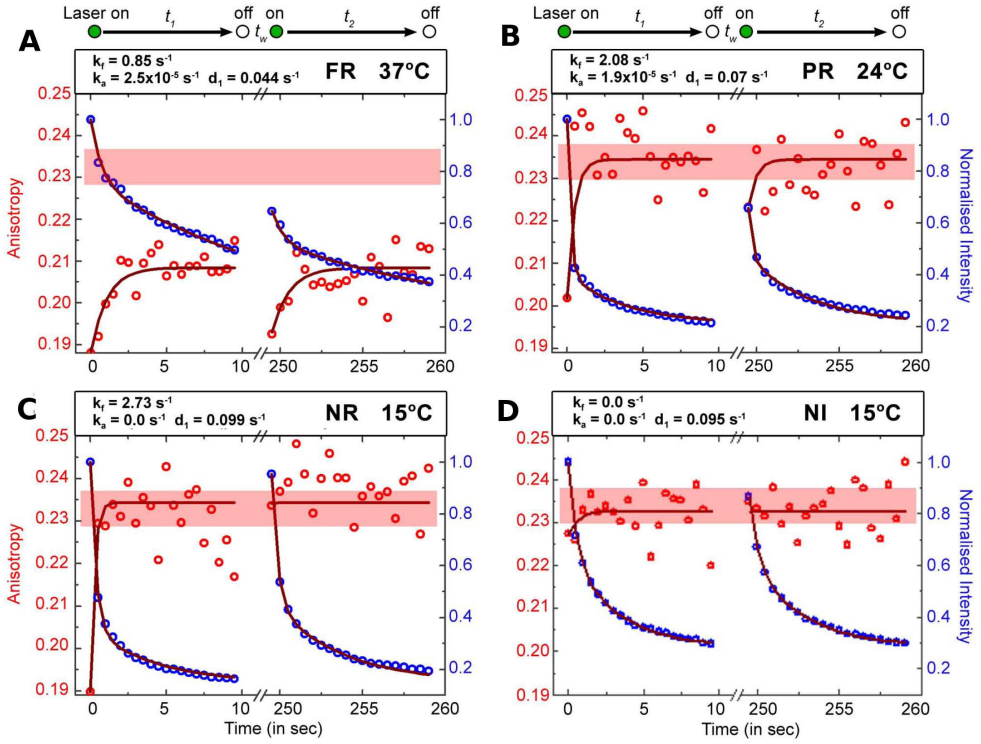

Figure 2.9: **Representative fits for each of the classes.** The panels A, B, C ad D contain intensity and anisotropy traces and fit parameters (k_a, k_f and d_1) for each of the classes FR, PR, NR and NI respectively.

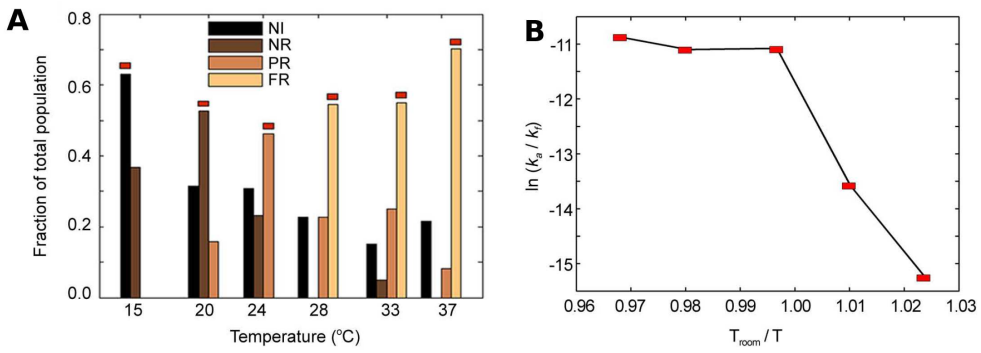

Figure 2.10: **Arrhenius Plot.** (A) Histogram representing the relative abundance of the class FR for 37^oC,33^oC and 28^oC, PR for 24^oC, NR for 20^oC and NI for 15^oC. (B) An Arrhenius Plot using the most probable values of the rates at these temperatures shows a switching behaviour at 24^oC.

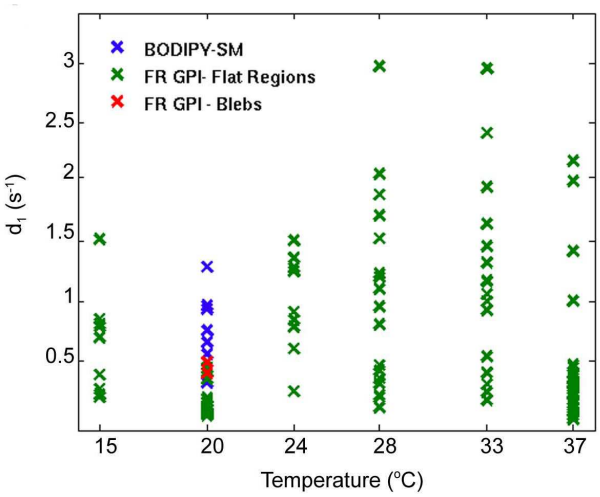

Figure 2.11: **Fit Parameter** d_1. The diffusion rate of a monomer d_1 obtained from the fits show a range of values. At 20^oC, the rates obtained for PLB labeled folate receptors on blebs and BODIPY labeled Sphingomyelin (short chain lipid) on flat regions are higher than the rate for FR-GPI in the flat regions.

2.4 Actin Remodelling: The retracting bleb

Freshly plated cells undergo rapid changes in their actin architecture in the process of adhering to a substrate. Part of the membrane locally rips off from the cytoskeleton and blebs out (Figure 2.12 A), to relax its high curvature content. Actin and myosin move into the bleb and attach onto the membrane. The contractility of the actomyosin complex causes the bleb to retract, until it becomes part of the bulk membrane again [14]. Tracking the area, actin concentration, and anisotropy of a retracting bleb, we first notice that actin which is initially absent in the bleb, slowly re-appears as a rim underneath the membrane, and remains there till retraction is complete. There are no clusters in the bleb when actin is absent, and clusters begin to reform after the rim of actin appears. This establishes a causal connection between actin, myosin activity, and cluster formation. The *speed* of bleb retraction (Figure 2.12 C) is a function of temperature, and shows a dependence reminiscent of the Arrhenius plot previously obtained, showing the common ground shared by the two separate processes.

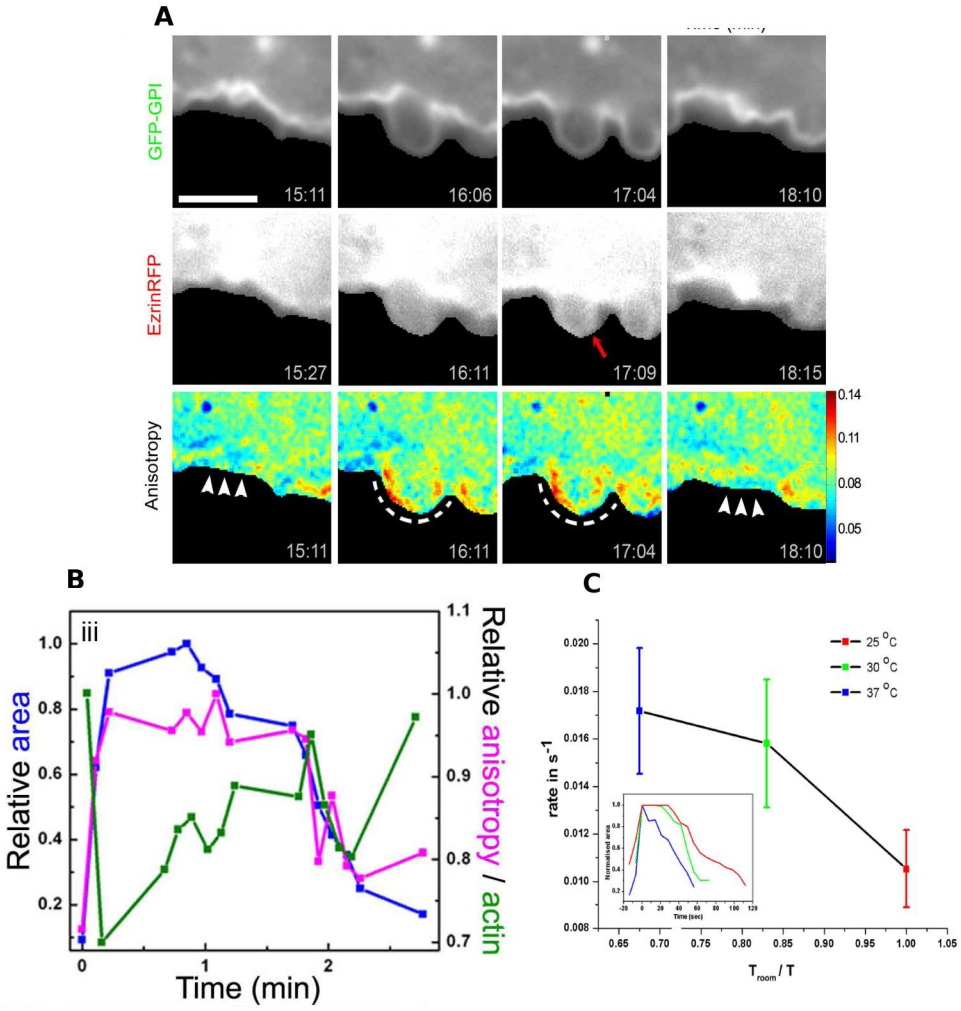

Figure 2.12: **The formation and retraction of a bleb on freshly plated fibroblasts.** (A) GFP labeled GPI-APs, RFP labeled Ezrin, a molecule that binds to polymerized actin and the anisotropy are followed as time progresses. A newly formed bleb contains very little actin and is devoid of nanoclusters (frame 2 in each of the panels). In less than a minute, a rim of actin begins to form, which causes the bleb to retract. (B) The anisotropy rapidly increases along with a rapid decrease in actin concentration when the bleb forms. as actin builds up in the bleb, the anisotropy recovers to its original value. (C) Rates of bleb retraction are sensitive to temperature, and seem to show the same trend as the Arrhenius curve previously obtained.

2.5 On Actin/Cholesterol Perturbation

It was found in the earlier study that cholesterol is required for the clustering of GPI-APs [38], due to its association with the lipid anchor of the proteins. The bleb retraction experiments implicates actin as well as a factor important for clustering. The cell is subjected to mild perturbations of cholesterol, and actin, and we look for differences in spatial arrangement as well as dynamics.

Cholesterol is perturbed using a reagent Methyl-β-cyclodextrin, a ring-like molecule that sequesters cholesterol and removes it from the membrane. Actin is perturbed using latrunculin and jasplakinolide, which interfere with the polymerization-depolymerization kinetics of actin filaments to change the overall actin content. Blebbistatin is known to block myosin activity, and is called so as it prevents the retraction of blebs. However, the microscopic nature of the perturbations is unimportant for our study, as we are interested in identifying the major players involved in the maintenance of GPI-AP features.

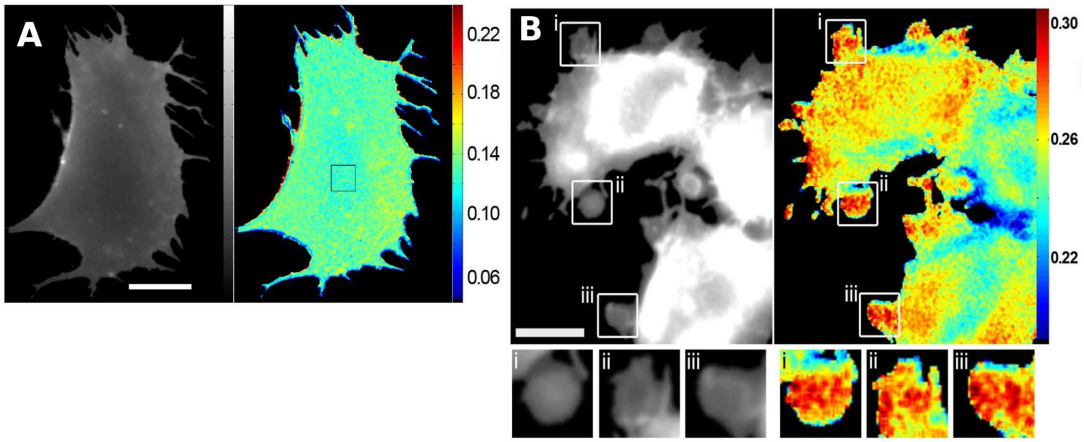

Figure 2.13: **Large scale changes in Morphology.** (A) Depleting the cell of small amounts of cholesterol using 10mM MβCD changes the morphology of the cell, enhancing the presence of spike like structures (B) Affecting the polymerization kinetics of actin using 14μM Jasplakinolide, gives rise to large blebs devoid of actin.

Depleting cholesterol removes most of the membrane heterogeneity in the flat regions of the membrane (Fig 2.13 A). Small protrusions like microvilli vanish, and the cell develops spike-like structures, presumably due to the clumping of actin bundles. The nanoclusters seem to be expelled to the periphery of the cell. The anisotropy distributions are narrow compared to control cells (Fig 2.14 A), indicating the loss of heterogeneity in the bulk.

The parameter ϕ, defined in subsection 2.2.2, decreases sharply (Figure 2.14 B), while the scales $\xi_1(\xi_2)$ progressively decrease(increase) (Figure 2.14 C and D), with MβCD concentration.

The removal of actin using strong concentrations of Lat or Jas induces the formation of blebs (Fig 2.13 B), devoid of nanoclusters. If the perturbation is removed, the blebs retract and the cell regains its original state.

To check for changes in dynamics, mild perturbations of actin and myosin are used, that do not cause large scale changes, but affect the local dynamics of actin. Perturbations of cholesterol, actin and myosin - all impede the reformation of clusters at 37^oC after photobleaching (Fig 2.15).

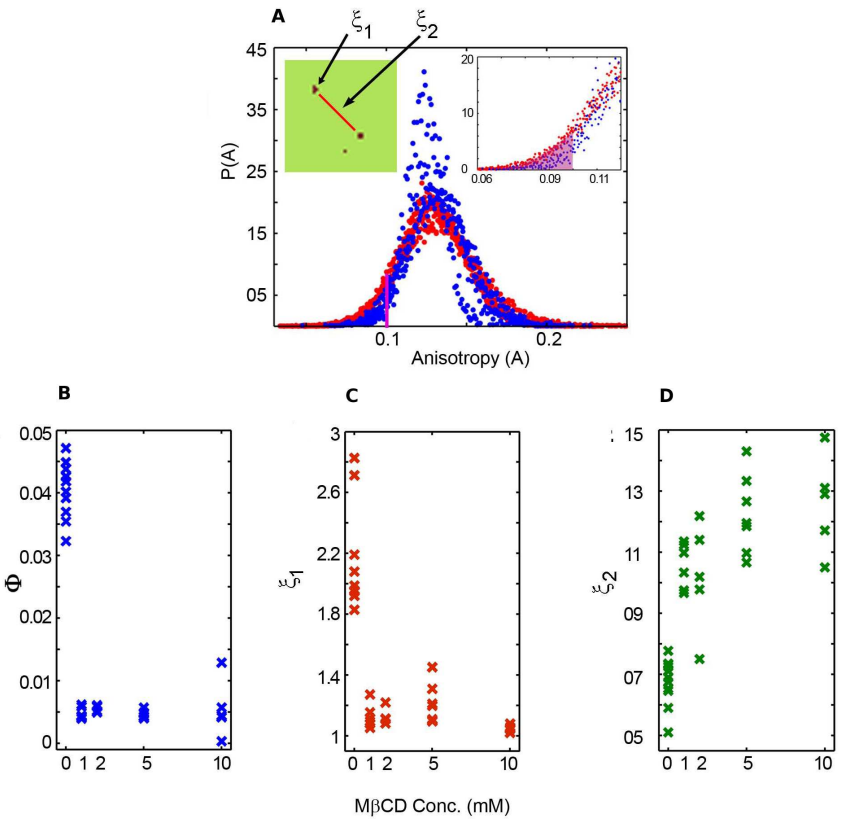

Figure 2.14: **Smaller scale changes on cholesterol depletion.** (A) The anisotropy distribution is narrow compared to control cells, when cholesterol (using 10mM MβCD) is depleted.(B) Accordingly, the fraction of pixels below A=0.1 decreases progressively on increasing MβCD concentration. (C and D) The average size of the regions decreases and the distance between them increases.

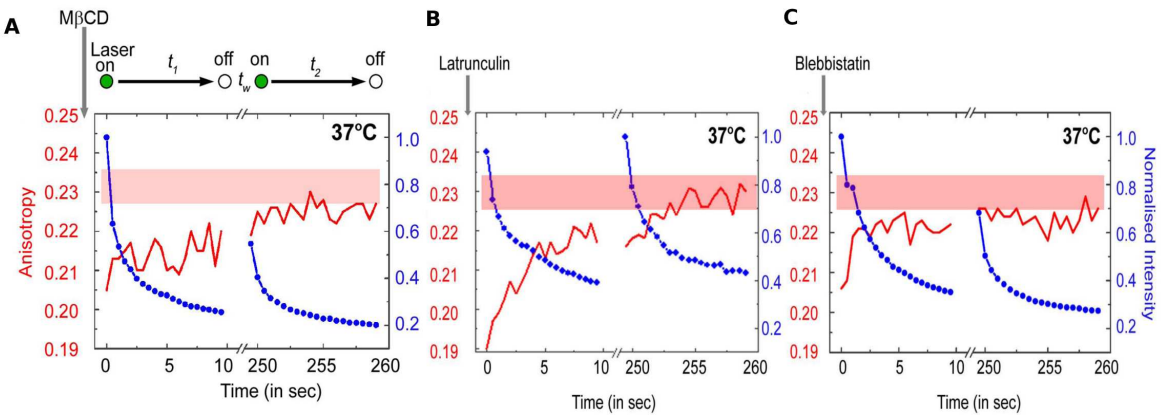

Figure 2.15: **Effect of perturbations on Dynamics.** The recovery of clusters at 37^oC is completely halted when (A)cholesterol, (B)actin or (C)myosin is perturbed.

2.6 Concluding Remarks

The experiments indicate that actin and nanoclusters may be related at various scales. Large scale features of anisotropy correlate with specific architectures of actin. It is possible that the small scale features, like the slowly decaying tails of the anisotropy distributions, are also maintained in some way by actin. Furthermore, the kinetics of nano-cluster formation is dependent on actin. Both the switching behaviours as well as the shape of the Arrhenius curve lead us to suspect that the formation-fragmentation kinetics of nanoclusters may be an active process, occurring due to active stresses applied by the actin cytoskeleton.

2.7 Appendix

The following are the expressions used in subsection 2.3.2.

$$
\begin{aligned}
C_{11}(\infty) &= \frac{(b+d_1)d_c i_c + d_c k_a i_c i_m + d_1 k_a i_m^2}{(b+d_1)(b+d_c+k_f)+(b+d_c)k_a i_m} \\
C_2(\infty) &= \frac{d_c k_f i_c + d_1(b+d_c+k_f)i_m}{(b+d_1)(b+d_c+k_f)+(b+d_c)k_a i_m} \\
C_{22}(\infty) &= \frac{2(b+d_1)d_c(b+d_c k_f)i_c + d_c k_a(2b+2d_c+k_f)i_m i_c + d_1 k_f(b+d_1+k_f)i_m}{2(2b+d_1+k_f)((b+d_1)(b+d_c+k_f)+(b+d_c)k_a i_m)} \\
B_{11} &= \frac{(d_1-d_c-k_f+k_a i_m)h_1 + 2k_a i_m h_2 + \Delta_c h_1}{\Delta_c} \\
B_{12} &= \frac{-(d_1-d_c-k_f+k_a i_m)h_1 - 2k_a i_m h_2 + \Delta_c h_1}{\Delta_c} \\
B_{21} &= \frac{-(d_1-d_c-k_f+k_a i_m)h_2 + k_f(2h_1+h_2) + \Delta_c h_2}{2\Delta_c} \\
B_{22} &= \frac{(d_1-d_c-k_f+k_a i_m)h_2 - k_f(2h_1+h_2) + \Delta_c h_2}{2\Delta_c} \\
B_{31} &= \frac{k_a i_m((-d_1+d_c-k_a i_m+\Delta_c)h_2 + k_f(2h_1+h_2))}{2\Delta_c(2b-d_1+d_c+k_f-k_a i_m+\Delta_c)} \\
B_{32} &= -\frac{k_a i_m((-d_1+d_c-k_a i_m+\Delta_c)h_2 + k_f(2h_1+h_2))}{2\Delta_c(2b-d_1+d_c+k_f-k_a i_m-\Delta_c)} \\
B_{33} &= \frac{b((2b+k_f)(b-d_1+k_f)-(2b+k_f)(b-d_1+k_a+k_f)i_m + d_1 k_a i_m^2)}{2(2b+k_f)(b(b-d_1+k_f)-k_a(b+k_f)i_m)}
\end{aligned}
$$

The rates are given by

$$
\begin{aligned}
r_1 &= -\frac{1}{2}(2b+d_1+d_c+k_f+k_a i_m-\Delta_c) \\
r_2 &= -\frac{1}{2}(2b+d_1+d_c+k_f+k_a i_m+\Delta_c) \\
r_3 &= -(2b+d_c+k_f)
\end{aligned}
$$

The terms that enter these are given by

$$
\begin{aligned}
i_m &= C_{11}(0) \\
i_c &= 2C_{22}(0) = 1 - i_m \\
h_1 &= -\frac{(b+d_1)d_c i_c + d_c k_a i_c i_m + d_1 k_a i_m^2}{(b+d_1)(b+d_c+k_f) + (b+d_c)k_a i_m} + C_{22}(0) \\
h_2 &= -\frac{d_c k_f i_c + d_1(b+d_c+k_f) i_m}{(b+d_1)(b+d_c+k_f) + (b+d_c)k_a i_m} + C_{11}(0) \\
\Delta_c &= \sqrt{(-d_1+d_c+k_f)^2 + 2k_a(d_1-d_c+k_f)i_c + k_a^2 i_m^2}
\end{aligned}
$$

Chapter 3

Architecture of Cortical Actin

In this chapter, we make attempts to understand the general principles guiding actin organization near the PM. As seen in the first chapter, cortical actin can be either horizontal ("H Actin") or vertical ("V Actin") with respect to the membrane, and these two architectures have very different effects on the PM. As seen in the previous chapter, the abundance of nanoclusters in a region depends on its local actin architecture. Therefore in order to understand molecular composition on the plasma membrane, it is imperative to first understand cortical actin.

3.1 H and V actin

Actin is an active polar filament that generates local stresses, either through its polymerization, or via its coupling to the myosin motor, as mentioned in the introduction. The active stress of a suspension of such filaments with polarization $\mathbf{p}(\mathbf{r}, t)$, can be found by viewing the actin filament as a force dipole [40], and is given by $\sigma_{ij} \propto p_i p_j$, to lowest order in $\mathbf{p}(\mathbf{r}, t)$. When such a suspension is bounded by a flexible, compressible surface, such as the plasma membrane, it generates normal as well as lateral stresses at the membrane (Figure 3.1). Since the membrane is flexible, a local normal stress will induce a local shape change, and a local lateral stress will result in local particle currents.

These statements present a picture for understanding the architecture of the cortical actin, just below the plasma membrane. We require the shape of the plasma membrane to be stationary in time. Each of the two architectures can achieve this in unique ways:

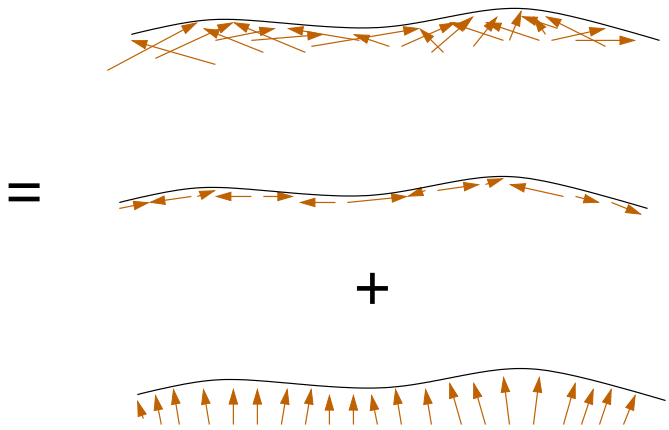

Figure 3.1: **Normal and Tangential Stresses at the membrane.** The stresses due to cortical actin at the plasma membrane can be resolved into tangential and normal components.

(1) **Aligned parallel to the membrane:** Such configurations of cortical actin do not result in normal forces at the membrane and hence do not protrude against the membrane. We refer to these configurations as H-actin. H actin locally creates density variations by subjecting molecules to forces along the polarization vector **p**. We will deal with H actin and its relationship with membrane composition in more detail in the next chapter.

(2) **Aligned perpendicular to the membrane**: As discussed in the introduction, polymerization of actin at a surface can rectify its motion and give it a velocity. A stationary shape is possible, only if the total normal force at the membrane is zero [31][20]. This can happen if depolymerization occurs when the growing actin makes contact with the membrane (Figure 3.2 (a)). A minimum gap of size corresponding to one monomer unit is therefore present between uncapped V-Actin and the membrane. Nucleation of actin sub units in this case, occurs away from the membrane, and polymerization occurs close to the membrane. If the nucleators of actin are instead present *at* the membrane, a non zero force due to stresses between the growing filaments and the bulk, is felt at the membrane, which can now cause a shape change. The resultant shape can be stationary only if the forces due to actin are balanced by the membrane restoring forces (Figure 3.2 (b)).

The cell can re-organize its cortical actin when it is subjected to stresses. We have encountered one such situation in the previous chapter, when blebs spontaneously form and retract as a cell is being plated. We are interested in the ways in which cortical actin architecture can be modulated - how, for instance, does the cortical actin change from

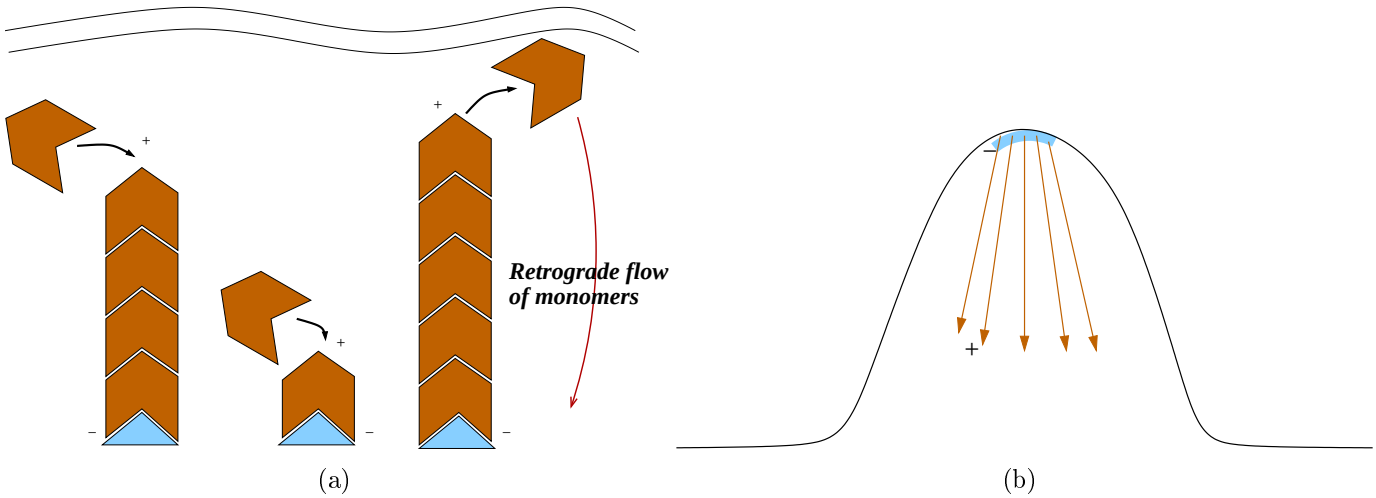

Figure 3.2: **Configurations of V actin**. (a) When nucleators (in blue) are present away from the membrane, V actin grows until it makes contact with the membrane, upon which it depolymerizes.(b) When nucleators are present at the membrane, V actin pushes against it, and a steady state results when the pushing force equals the membrane's shape restoring force.

predominantly H-Actin to V-Actin? We will see in the next section that the answer to this question lies in the molecular players involved in establishing the two architectures of actin.

3.1.1 Chemical network evidence

From the above arguments we can reconcile the connections between flat regions and horizontal actin, protrusions and vertical actin, encountered in the previous chapter. Since horizontal actin can generate lateral stresses and vertical actin cannot, the membrane compositions associated with these structures should also be different.

3.1.1.1 Actin, GPI-AP organization and GEEC endocytosis

Sharma et al [38]showed that the nanoclustering of GPI-APs is a prerequisite for their endocytosis via the GEEC pathway. Crosslinking of these proteins with antibodies prevents their uptake via the GEEC pathway. Chadda et al [13] show that the prevalence of endocytosis depends on actin activity. By interfering with the polymerization machinery of actin, they observed an inhibition of endocytosis. Finally, the experiments described

in the previous chapter highlight the relationship between nanoclustering and actin activity. Microvilli, lamellipodia and filipodia, where actin filaments protrude towards the membrane, are poor in nanoclusters, while the flat regions of the membrane, where the actin is predominantly tangential to the membrane, are rich in nanoclusters. Endocytosis, Nano-clusters and Actin configurations are therefore causally linked and these three studies point to actin and its morphology/behaviour to be the initiator of both nanoclustering and well as endocytosis. Increased endocytosis, is a signature of locally horizontal actin, as is a high fraction of nanoclusters. In short, we can prescribe the following thumb rules:

- Many nanoclusters, H actin, high endocytosis.
- Few nanoclusters, V actin, low endocytosis.

We are already aware of the spatial heterogeneity of both actin architecture as well as cluster concentration, and the correlation between the two. It is conceivable that this heterogeneity is reflected in the local propensity for endocytosis as well.

3.1.1.2 CDC42 and ARF1, two modulators of endocytosis.

A recent study [27] showed that two GTPases, CDC42 and ARF1, can toggle between low and high uptake via GEEC endocytosis, by their relative presence in an activated membrane bound form. Furthermore, the relative concentrations of these two molecules, in their activated forms, are mediated by a third molecule ARHGAP10, that contains domains that bind to both CDC42 as well as ARF1. The following table summarizes the results of of their experiment. The perturbed species are indicated by the red arrows, where perturbation can either increase (up arrow) or decrease (down arrow) their membrane bound levels. The effect of this perturbation can either increase, or decrease the read-out (black arrows). In some cases, simultaneously perturbing two species, reverses the effect of one and one sees no change (-) in the readout.

ARHGAP10	ARF1	CDC42	Endocytosis
	↑		↑
	↓	↑	↓
↓			↓
↓	↑		–
		↑	↓
	↑	↑	–

Table 3.1: **Perturbations (in red) and Readouts (in black)**

In short, again,

- High activated ARF1, high endocytosis, and therefore H actin;
- High activated CDC42, low endocytosis, and therefore V actin;

Kumari et al [27] proposed the following model (Figure 3.3) for the working of these three players: Arf1, on activation, binds to the plasma membrane, and consequently recruits ARHGAP10 to the membrane. The ARF-GAP complex deactivates CDC42 more efficiently, leading to its unbinding from the membrane. ARHGAP10 is therefore a mediator between high and low activated levels of the two species.

3.1.2 Morphological evidence

CDC42 in its activated membrane bound form, signals the recruitment of the actin polymerization machinery at the plasma membrane. This activation results in the formation of filipodial structures and microspikes, characterized by the protrusive bundles of actin below the membrane [1].

In contrast, reduction in activated ARF1, leads to the formation of microspikes, similar in actin morphology to microvilli, filipodia, lamellipodia, all structures that are formed out of locally enhanced CDC42 levels. ARF1 is also know to localize on actin patches in the Golgi [12].

We are prompted by the observations, to call CDC42 and ARF1 'recruiters' of vertical and horizontal actin respectively. These molecules may or may not act in conjunction with other players, but we can take all molecules that, along with CDC42, are responsible for actin bundling, and club them into a single group and call it 'V-Actin Recruiting

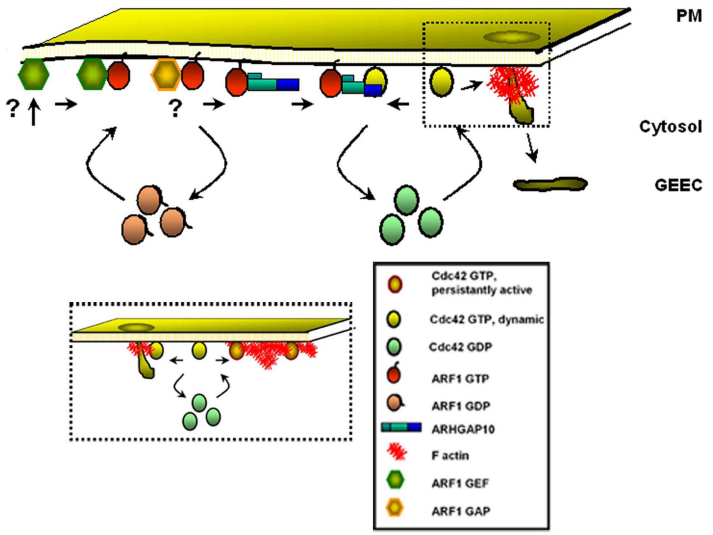

Figure 3.3: **Proposed model for the interaction of the two GTPases via ARHGAP10**

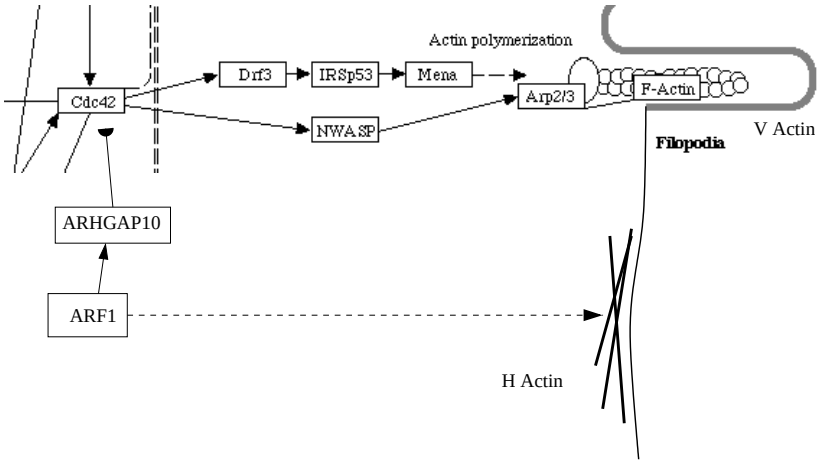

Figure 3.4: **Sub-network of the actin cytoskeleton regulation machinery** (Courtesy http://www.genome.jp/dbget-bin/show_pathway?map04810) Activated CDC42 , brings about the recruitment of various molecules that ultimately leading the polymerization of V actin at the membrane .Activated ARF1 may either aid in the recruitment of H actin at the membrane or in the inhibition of CDC42 (as indicatedby the flat arrowhead)

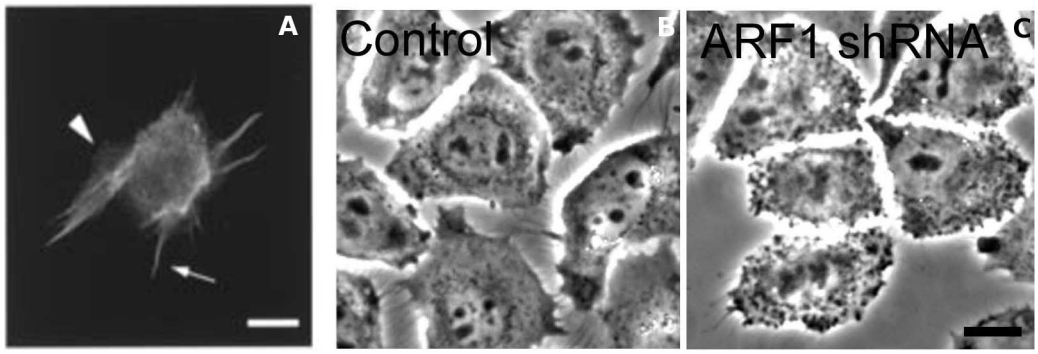

Figure 3.5: **Formation of microspikes** (A) upon activation of CDC42 [23] (B) upon reduction of ARF1 [27]

Machinery'. Similarly ARF1 and its co-players can be clubbed into 'H-Actin recruiting machinery'. These two groups talk to each other via ARH-GAP10.

3.1.3 Mechanism of toggling

GTPases in the cell, are proteins that contain a tightly bound guanine nucleotide GTP. The cell frequently uses GTPases as "molecular switches", due to the conformation change that they undergo on the hydrolysis of GTP [1]. Most of the time, these proteins are found in their inactive, GDP bound form. They become active when they exchange their GDP for a GTP molecule. The activation of the GDP bound form occurs when it encounters a Guanine Nucleotide Exchange Factor (GEF), which binds the inactive molecule, inducing it to release its bound GDP. The vacant binding site is quickly occupied by GTP, present in abundance in the cytosol. This event usually occurs as a response to extracellular signals. An activated GTPase is inactivated by the action of another protein called a GAP (GTPase activating protein). A bound GAP can induce the GTPase to hydrolyze its GTP molecule to GDP (and inorganic phosphate), which remains tightly bound to the parent protein.

In many cases, such as the present one, the conformation change induced in the activated GTPase enables it to bind to the membrane. Such molecules therefore can move between the membrane and cytosol on the action of GAPs and GEFs.

We denote ARF1 and CDC42 by C_1 and C_2, their activated forms by C_1^* and C_2^*, ARHGAP10 by H and the ARF-GAP complex as P. Activation of both C_1 and C_2

are catalyzed by GEF_1 and GEF_2 and follow a standard Michelis Menten kinetics[6]. Similarly deactivation is catalyzed by GAP_1 and P and also follow Michelis Menten kinetics.

The complete network of reactions is given by

$$
\begin{array}{rcccl}
 & \overset{g_1}{\underset{g_{-1}}{\rightleftharpoons}} & T_1 & \overset{g_1'}{\rightarrow} & \\
C_1 + GEF_1 + GTP & & & & C_1^* + GEF_1 + GDP \\
 & \overset{h^+}{\underset{h^-}{\rightleftharpoons}} & & & \\
C_1^* + H & & & & P \\
 & \overset{p_1}{\underset{p_{-1}}{\rightleftharpoons}} & I_1 & \overset{p_1'}{\rightarrow} & \\
C_1^* + GAP_1 & & & & C_1 + GAP_1 \\
 & \overset{g_2}{\underset{g_{-2}}{\rightleftharpoons}} & T_2 & \overset{g_2'}{\rightarrow} & \\
C_2 + GEF_2 + GTP & & & & C_2^* + GEF_2 + GDP \\
 & \overset{p_2}{\underset{p_{-2}}{\rightleftharpoons}} & I_2 & \overset{p_2'}{\rightarrow} & \\
C_2^* + P & & & & C_2 + P
\end{array}
$$

Where T_1, T_2, I_1 and I_2 are all intermediates in the catalysis reactions.

This complicated network can be considerably simplified by assuming that the cyctosolic forms of C_1 and C_2 are very large in number and can behave as constant sources, replenishing their activated forms. Michelis Menten kinetics for activation implies that C_1^* and C_2^* are both produced at a constant rate, independent of substrate concentrations (C_1 and C_2). The de-activation cycle however, involves a finite concentration of substrate molecules (C_1^* and C_2^*), and the rate of formation of the product (C_1 and C_2) varies linearly with substrate concentration. The simplest network that incorporates all the features of the players is illustrated in Figure 3.6. We have here done away with all the intermediate states, assuming the observation time window of the reaction is much larger than the lifetime of these intermediate states. Catalysis is therefore, in this network, a one step unidirectional process. The deactivation of C_2 however, is catalyzed by a product of another sub-reaction (P), and therefore depends on the concentration of this

product. The toggler P in our model, is assumed to be restricted in concentration, and satisfies the conservation law

$$H + P = K$$

The rate equations for this simple system are

$$\begin{aligned}
\frac{dC_1^*}{dt} &= v_1 - \bar{p_1} C_1^* - h^+(K-P)C_1^* + h^- P \\
\frac{dP}{dt} &= h^+(K-P)C_1^* - h^- P \\
\frac{dC_2^*}{dt} &= v_2 - \bar{p_2} P C_2^*
\end{aligned}$$

The rates in the simpler network are related to the rates in the larger network in the following way

$$\begin{aligned}
v_1 &= \frac{g_1'[GEF_1][C_1]}{K_{M1} + [C_1]} \\
v_2 &= \frac{g_2'[GEF_2][C_2]}{K_{M2} + [C_2]} \\
\bar{p_1} &= \frac{p_1'[GAP_1]}{K_{M1}^-} \\
\bar{p_2} &= \frac{p_2'}{K_{M2}^-}
\end{aligned}$$

where $K_{M1} = (g_{-1} + g_1')/g_1$, $K_{M2} = (g_{-2} + g_2')/g_2$,$K_{M1}^- = (p_{-1} + p_1')/p_1$ and $K_{M2}^- = (p_{-2} + p_2')/p_2$ and the square brackets indicate concentrations of the bracketed species. We restrict ourselves to this simple network as it is more tenable for inclusion of spatial degrees of freedom, which we intend to pursue further.

The simple network supports only one steady state:

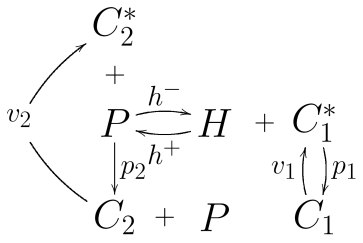

Figure 3.6: **A Simplified Network of The Reactions**

$$
\begin{aligned}
C_1^*(\infty) &= \frac{v_1}{\bar{p_1}} \\
C_2^*(\infty) &= \frac{v_2(C_1^*(\infty)+\alpha)}{\bar{p_2}C_1^*(\infty)K} \\
P(\infty) &= \frac{C_1^*(\infty)K}{C_1^*(\infty)+\alpha}
\end{aligned}
\tag{3.1}
$$

where $\alpha = h^-/h^+$. The larger network involving finite concentrations of all the players, does not differ qualitatively from the simple network. Detailed analysis of the larger network revealed that it supported one physical steady state as well. The number of control parameters is also the same (4). $C_2^*(\infty)$ has an inverse relationship with $C_1^*(\infty)$. Plotting the normalized difference $\phi = (C_2^*(\infty) - C_1^*(\infty))/(C_2^*(\infty) + C_1^*(\infty))$ against K and against $C_1^*(\infty)$ (Figure 3.7), we see that at low values of α, increasing the ARHGAP10 availability K can take us from a regime where activated CDC42 dominates ($\phi \sim 1$) to one where activated ARF1 dominates ($\phi \sim -1$).

3.2 Qualitative Phase Diagram

From the results, it is clear that ARF1 and ARHGAP10 control the levels of CDC42. For actin architectures, it means that decreasing the amount of H actin locally increases the amount of V actin. In response to a stimulus, the cell presumably has a mechanism (not included here), the effect of which is subsumed in the parameter $v_1/\bar{p_1}$, that can regulate the levels of H actin. Similarly, low levels of H actin, allow the polymerization of V actin. There is a possibility of another phase where the levels of both H and V actin are low. This phase is attainable if we include one more step in the network, the formation of an

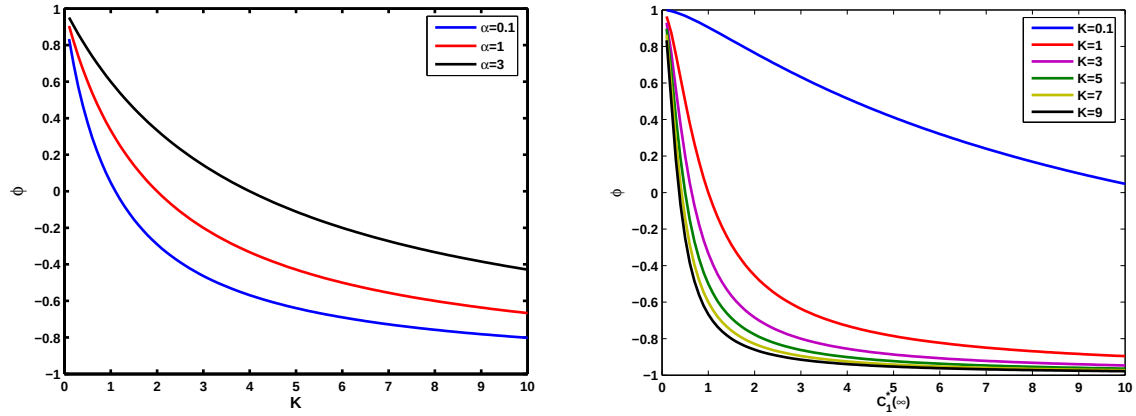

(a) (b)

Figure 3.7: **The order parameter ϕ, switching between high and low levels of CDC42** (a) as a function of ARHGAP10 availability, for various values of α, at $v_1/\bar{p_1} = v_2/\bar{p_2} = 1$ (b) as a function of ARF1 ($C_1^*(\infty)$) for various value of K, at $v_2/\bar{p_2} = 1$, $\alpha = 1$.

intermediate between CDC42 and its GAP (ARF1-ARHGAP10). Figure 3.8 illustrates this extended network.

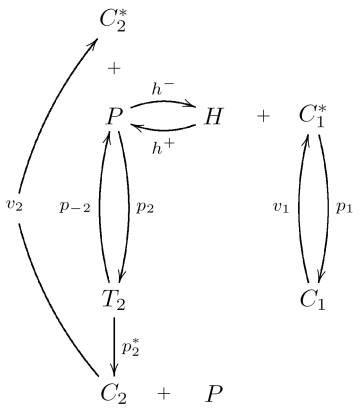

Figure 3.8: **Including one more arm in the network**

At a very low Michelis constant K_{M2}^-, the intermediate state T_2 forms a sink for both ARF1 and CDC42. With this full network we expect a phase diagram that contains the phases (High H actin, Low V actin) - corresponding to the flat regions of the cell, (Low H actin, High V actin) - corresponding to microvilli, lamellipodia etc, and (Low H actin, Low V actin) -corresponding to blebs. The following qualitative phase diagram (Figure

3.9) summarizes our claim.

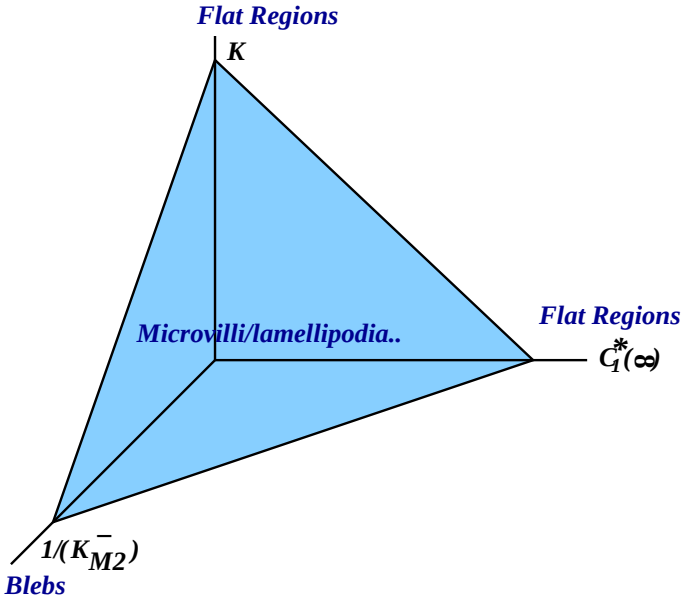

Figure 3.9: **Qualitative Phase Diagram of actin architectures**

3.3 Concluding Remarks

The two recruiting machineries of actin interact via a third molecular player, thereby allowing the cell to control its local cortical actin architecture. The toggle network proposed in this chapter deals with two particular GTPases that have opposing effects. It is possible that this simple mechanism forms a general route via which two such GTPases can interact, and is therefore a possible network "motif" that involves a minimum number of players.

Chapter 4

The Active Composite Membrane

4.1 Membrane, Actin and Myosin

The complex molecular organization on cell membranes could arise from

- A highly heterogeneous but isolated membrane (the fluid mosaic model, the conventional raft model)
- Membrane interactions with a static skeleton of cross-linked filaments (the skeleton fence model)

In the former, molecules freely diffuse in membrane patches of varying diffusivity, and in the latter, molecules can be 'corralled' together by the cortical actin meshwork. Chapters 2 and 3 describe the sequence of experiments that lead us to believe that membrane composition is dependent on cortical actin architecture. The GPI-AP cluster densities show large variations over different actin architectures ; the formation of clusters also requires myosin activity, as demonstrated by the retracting bleb. A complete model of particle dynamics on the membrane should primarily contain a mechanism for the formation of a static cluster, in a way that violates the law of mass action. Secondly, it should replicate the qualitative steady state features of the experimental results, like the exponential tails of the anisotropy distributions. It should finally, provide an explanation for the *dynamics* of clusters and the switching behaviour of the Arrhenius curve.

The fluid mosaic model does not take actin into account at all, and the skeleton fence model explains anomalies in particle motion over the scale of 100's of nanometers. Neither

of the two models can adequately describe the *nano-scale* organization of GPI-AP's. In this chapter, we propose a model of membrane particle dynamics that takes into account the effects of an active substrate of cross-linked actin filaments, and this leads to the notion of an Active Composite Membrane.

4.2 Dynamics of filaments and active cross linkers

4.2.1 The long and short of it.

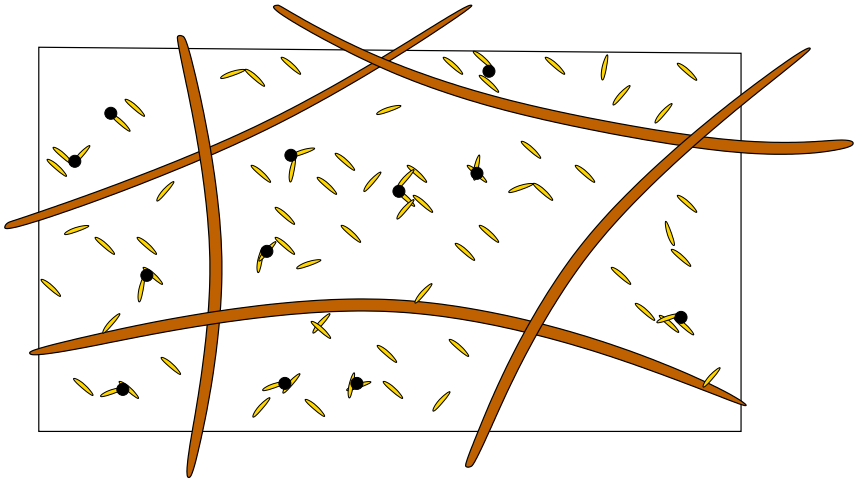

(a) The underside of an Active Composite Membrane : a membrane (white patch) supported on static filament skeleton (in brown) , and driven out of equilibrium by forces exerted by an actively re-modelling shell of short filaments (in gold) crosslinked by myosin (in black)

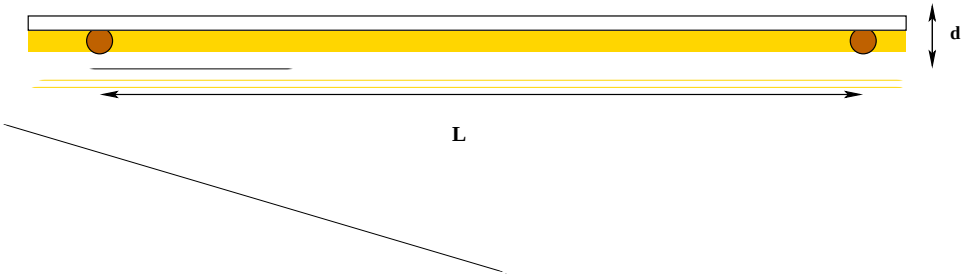

(b) Lateral view of a section of an Active Composite Membrane , with a mesh-size L and a thickness d.

Figure 4.1: **Long and short filaments**

Cryo-electron micrographs of the cortical actin adjoining the cell surface, suggest the existence of a relatively static, crosslinked meshwork of mesh-size $L \sim 200$nm[32]. The

clusters of GPI-APs however, exist over scales of nanometers, and fragment over a time ~ 0.1 seconds [19]. In order to link GPI-AP and actin behaviour, we make the following proposition: In addition to the observed long and static filaments, there exist short and fast filaments in a shell of thickness $\sim d$ below the membrane. The short filaments are linked together by myosin proteins, machines that render the filaments 'active' by transduction of ATP, giving rise to active forces.

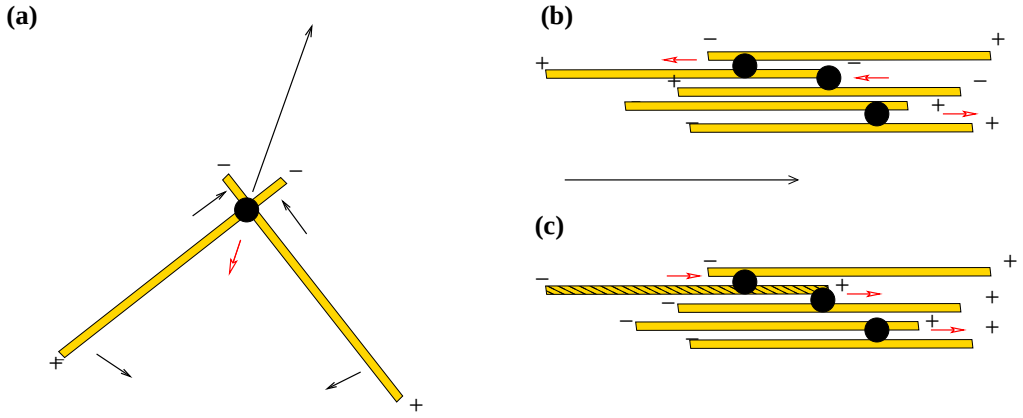

Figure 4.2: **The action of myosin cross-linking.** (a) Myosin moves from the '-' to the '+' ends of the filaments it binds (along the red arrow) causing the pair to move along the black arrow. (b) A bundle of filaments pointing in various directions.(c) A bundle of aligned filaments. In both these cases the effective velocity of the bundle is along the black arrow.

Many theoretical studies ([40, 44, 22, 37, 28, 33, 35, 10]) of suspensions of actin and myosin are based on the assertion that the active forces in principle include all contributions that are not disallowed by symmetry. The contributions do not have the conventional constraints of equilibrium physics: they need not be derivable from a free energy, and no constraints (eg like moduli of elastic distortions being positive) bind the coefficients. These active forces then give rise to active fluxes in the hydrodynamic equations of motion. Additionally, the noises in the equations of motion need not obey fluctuation dissipation theorem.

A.Ahmadi et al [9] provide a more detailed mechanical framework, for calculating the effect of myosin cross linking at large length scales and time scales much larger than the binding-unbinding time of myosin. They consider a microscopic model where the walking of a cross linker on the two filaments that it straddles, causes the two filaments to translate and rotate with respect to each other and the solvent. The myosin cross linker walks from the '-' end to the '+' end of the filament. Figure 4.2 shows the effect of

cross-linker walking on a pair of filaments. When the cross linker steps along the filaments in the direction of the red arrow (Fig 4.2(a)), it exerts a force on the filaments in the opposite direction which causes the crosslinked filaments to move with respect to the viscous membrane environment with a velocity v, and with respect to each other with a velocity v_r. The fixed size of the motor requires that the two filaments rotate with respect to each other with a relative angular velocity ω when stepping occurs. The microscopic model prescribed in [9] expresses v, v_r and ω as a function of the mean stepping rate of myosin β', the maximal spatial variation of the stepping α' and the active torsional modulus of the cross linker γ'.

A group of filaments bound pair-wise with myosin can have an effective velocity with respect to the solvent depending on the distribution of polarities of the filaments. In Figure 4.2(b), the average filament velocity (black arrow) is a combined effect of the stepping of all the motors in the bundle. When the polarity of all the filaments in the bundle are the same, a filament at the periphery (the patterned filament in Figure 4.2(c)) of the bundle aligns along and moves *up* a gradient of filament concentration. This is what characterizes the acto-myosin complex are 'contractile'.

The authors of [9] go on to coarse grain the microscopic equations to obtain equations of motion for the hydrodynamic variables of the problem. Their equations of motion are consistent with the symmetry obeying phenomenological equations. In this study, we adopt the former philosophy of writing down the equations of motion based on symmetry arguments for a system of actively crosslinked filaments interacting with a flat, stiff membrane.

4.2.2 Hydrodynamic variables

In addition to the action of myosin, actin filaments also constantly polymerize and depolymerize. Myosin can also bind and unbind from actin filaments. We assume in the current study, that the time scales of polymerization-depolymerization and myosin binding-unbinding, are both much larger than the time scales of motion and organization of the the filaments, and therefore both the length of the filaments and the number of bound myosin motors are effectively constant. Another "small" time scale is the appearance and disappearance of the short filaments at the membrane, resulting in a constant concentration of short filaments at the membrane. With these assumptions, the conserved variables in the problem are $c(\mathbf{r}, t)$, the concentration of short filaments of constant length, and

$C(\mathbf{r})$, the concentration of the large filaments. Rotational symmetry in the plane of the membrane is broken by the average orientation of the short filaments $\mathbf{n}(\mathbf{r},t)$ (pointing toward the minus ends of the filaments), and of the long filaments $\mathbf{N}(\mathbf{r})$, defined by the following equations:

$$\begin{aligned} p(\mathbf{r},t) &= c(\mathbf{r},t)\mathbf{n}(\mathbf{r},t) = (1/V)\sum_i \mathbf{n_i}\delta(\mathbf{r}-\mathbf{r}_i(t)) \\ P(\mathbf{r}) &= C(\mathbf{r})\mathbf{N}(\mathbf{r}) = (1/V)\sum_i \mathbf{N_i}\delta(\mathbf{r}-\mathbf{R}_i) \end{aligned} \tag{4.1}$$

where i labels the filament and V is an elemental coarse graining area. Based on the "long-static" assumption, the concentration and orientation of the long filaments are constant in time. The hydrodynamic variables are therefore $c(\mathbf{r},t)$ and $\mathbf{n}(\mathbf{r},t)$.

4.2.3 Equations of motion

The concentration $c(\mathbf{r},t)$ of filaments, as stated earlier, is a conserved quantity and hence should obey a continuity equation. The current of filaments combines the average centre of mass velocity v due to the walking of myosin, as well as diffusion of the centre of mass coordinate. In the vicinity of static filaments, myosin can couple short filaments adjacent to the long static filaments, resulting in an effective filament velocity v' along $\mathbf{N}$. The total current therefore contains an advective contribution due to the long static filaments as well.

$$\partial_t c = -\nabla\cdot[vc\mathbf{n} + v'cC\mathbf{N} - D_f\nabla c] + f_c \tag{4.2}$$

Let us note here that we do not take into account the variation in diffusion coefficient due to the shape anisotropy of the actin filament, and assume that the effective diffusion constant D_f, is that of the centre of mass of the filaments. D_f is the trace of the diffusion matrix [2],

$$\mathbf{D} = D_{\|}\mathbf{nn} + D_{\perp}(\mathbf{I}-\mathbf{nn}) \tag{4.3}$$

For a dilute solution of long thin rods $D_{\perp} = D_{\|}/2 = D_f/2$ and $D_f = k_B T log(\ell/b)/(2\pi\eta\ell)$

(η is the solvent viscosity, and ℓ and b are the length and diameter of the filaments, respectively).

The equation for $\mathbf{n}$ is a generalization of the nematohydrodynamic equations for a suspension of polar filaments [3]. In conventional nematohydrodynamics, the ambient fluid velocity field $\mathbf{v}$, aids in aligning the polarization along the flow via the contribution $(\mathbf{v}\cdot\nabla)\mathbf{n}$. In a suspension of *active* filaments, the dominant contribution to the ambient fluid velocity comes from the active stresses due to acto-myosin. The hydrodynamic velocity can be treated within a local friction approximation, coming from a mobility times the divergence of the active stress tensor $\sigma_{ij} = Wcp_ip_j$.

$$\mathbf{v} \;=\; -\Gamma\nabla\cdot\sigma \tag{4.4}$$

Where $1/\Gamma$ is an effective friction coefficient due to the static filament meshwork. From the above equation , we see that the contributions of fluid velocity to the orientation are of higher order in the fields and derivatives. Hence we do not include them in the equation of motion for $\mathbf{n}$. Terms that resemble the conventional flow-alignment due to the fluid, are however present purely from symmetry considerations. These include $\lambda(\mathbf{n}.\nabla)\mathbf{n}$, $\lambda_1\nabla|\mathbf{n}|^2$ and $\lambda_2\mathbf{n}\nabla\cdot\mathbf{n}$. In this active scenario, these coefficients are not restricted by Galilean invariance to be 1.

Symmetry requires that $\partial_t\mathbf{n}$, should contain a term proportional to ∇c. This contribution aids in aligning the polarization along gradients of the filament concentration field, an effect that can be termed 'self-anchoring'. The equation for $\mathbf{n}$ is

$$\begin{aligned}\partial_t\mathbf{n} + \lambda(\mathbf{n}\cdot\nabla)\mathbf{n} + \lambda_1\nabla|\mathbf{n}|^2 + \lambda_2\mathbf{n}\nabla\cdot n + \mu(\mathbf{N}\cdot\nabla)\mathbf{n} = \\ K\nabla^2\mathbf{n} + \delta K\nabla(\nabla.\mathbf{n}) + \alpha(\bar{c}-c^*)\mathbf{n} - \beta|\mathbf{n}|^2\mathbf{n} + \zeta\nabla c + AC\mathbf{N} + \mathbf{f_n}\end{aligned} \tag{4.5}$$

The first two terms on right hand side of (4.5) resemble the restoring forces arising from bend distortions of energy $\int dAK(\nabla\times\mathbf{p})^2$ and splay distortions of energy $\int dA(K+\delta K)(\nabla\cdot\mathbf{p})^2$[3]. As pointed out in [9], when myosin is involved, K is an active parameter related to α', β' and γ'(as mentioned earlier), while δK is related to the excluded volume of the filament pair. The sum $\alpha(\bar{c}-c^*)\mathbf{n} - \beta|\mathbf{n}|^2\mathbf{n}$ functions as a soft potential that ensures that filaments are locally ordered above a critical concentration c^*.

4.2.3.1 Effect of the Long Static filaments

The long static filaments enter the equations of motion via an advective current of filaments at the boundary between the two species, a term resembling flow-alignment $\mu(\mathbf{N}\cdot\nabla)n$ and a field $AC\mathbf{N}$, aligning $\mathbf{n}$ along $\mathbf{N}$.

If we observe a patch of membrane whose size is much smaller than the mesh size, the effects of the long static meshwork enter the equations of motion as boundary conditions. In the concentration equation, it enters as a flux parallel to the boundary, and in the orientation equation, a field at the boundary. The boundary effects are unimportant beyond a distance of one bend correlation length into the membrane.

If the patch of membrane under consideration is however much larger than a mesh size, the effects of the the long static meshwork appear as a "quenched random field". We assume that the effects of this field are felt by the short filaments only in the *mean*. Reflecting the random orientations of the long static filaments, the mean of all terms containing $\mathbf{N}$ is therefore effectively zero.

4.2.3.2 Final equations of motion

Following [44], of the three terms $\lambda(\mathbf{n}.\nabla)\mathbf{n}$, $\lambda_1\nabla|\mathbf{n}|^2$ and $\lambda_2\mathbf{n}\nabla\cdot\mathbf{n}$, we retain only the first. We do so as this term is the only purely active contribution to the advection, the others being derivable from a free energy.

Based on the above statements, we arrive at the following equations of motion for the short filaments :

$$\begin{aligned}\partial_t c &= -\nabla\cdot(vcn - D_f\nabla c) + f_c \\ \partial_t n &= K\nabla^2 n + \delta K\nabla(\nabla\cdot n) + \zeta\nabla c + \alpha(\bar{c}-c^*)\mathbf{n} - \beta\mathbf{n}|\mathbf{n}|^2 + \mathbf{f_n}\end{aligned} \tag{4.6}$$

We will elaborate on the sources of noise f_c and $\mathbf{f}_n$ in section 4.3.

4.2.4 Linear Stability Analysis about homogeneous phases

A combination of linear stability analysis and numerical solutions of the equations of motion is used to obtain the full phase diagram. Linear stability analysis will reveal the

nature of the instabilities in this system, if present. Perturbations $\{\delta\mathbf{n}, \delta c\}$ are added to a variational ansatz steady state $\{\mathbf{n}, c\}$ and the equations of motion are expanded upto linear order in $\{\delta\mathbf{n}, \delta c\}$. The equations of motion are then expressed in terms of the Fourier modes of the perturbations $\delta n_{x,k} = \int \delta n_x(\mathbf{r}) e^{-i\mathbf{k}.\mathbf{r}} dr$, $\delta n_{y,k} = \int \delta n_y(\mathbf{r}) e^{-i\mathbf{k}.\mathbf{r}} dr$ and $\delta c_k = \int \delta c(\mathbf{r}) e^{-i\mathbf{k}.\mathbf{r}} dr$, and are finally cast as

$$\partial_t \begin{pmatrix} \delta n_{x,\mathbf{k}} \\ \delta n_{y,\mathbf{k}} \\ \delta c_{\mathbf{k}} \end{pmatrix} = \mathbf{A} \cdot \begin{pmatrix} \delta n_{x,\mathbf{k}} \\ \delta n_{y,\mathbf{k}} \\ \delta c_{\mathbf{k}} \end{pmatrix} \tag{4.7}$$

The eigenvalues of A, when positive lead to the growth of instabilities. Numerical solutions are obtained by implicitly evolving $\{\mathbf{n}, c\}$ according to the equations of motion using the alternating direction operator splitting method [7]. The spatial discretization in our numerical treatment is taken to be $\Delta x = 1$ and the the equations are evolved with a time step $\Delta t = 0.01$. Periodic boundary conditions are employed, and we work with system sizes much larger than the bend correlation length $\sqrt{K}$.

4.2.4.1 Stability about the homogeneous disordered state

In this case,

$$\mathbf{A} = \begin{pmatrix} \bar{\alpha} - k_x^2(K + \delta K) - Kk_y^2 & -k_x k_y \delta K & ik_x\zeta \\ -k_x k_y \delta K & -\bar{\alpha} - k_y^2(K + \delta K) - Kk_x^2 & ik_y\zeta \\ -ik_x v & -ik_y v & -D_f k^2 \end{pmatrix} \tag{4.8}$$

where $\bar{\alpha} = \alpha(\bar{c} - c^*)$ and $k = \sqrt{k_x^2 + k_y^2}$. The eigenvalues of $\mathbf{A}$ are $\mu_1 = \bar{\alpha} - k^2 K$, $\mu_{2/3} = \frac{1}{2}(\bar{\alpha} - k^2(K + D_f + \delta K) \pm \sqrt{(\bar{\alpha} + k^2(D_f - K - \delta K))^2 + 4k^2\zeta v})$.

When the filament concentration $\bar{c}$ is less than the critical concentration c^* and when $\zeta v > -D_f\bar{\alpha}$, the eigenvalue μ_3 is positive for a band of wavelengths. At the threshold of this instability, the coupled effect of self-anchoring and advection, which we call the 'contractility' ζv, overcomes diffusion to form stable concentration modulations. From linear stability analysis, the growth rate of the modulations is maximum (Figure 4.3) for the wavenumber

$$k_d = -\bar{\alpha}\sqrt{\frac{D_f\bar{\alpha}+\zeta v}{2\zeta v((D_f-(K+\delta K))\bar{\alpha}+\zeta v)}} \tag{4.9}$$

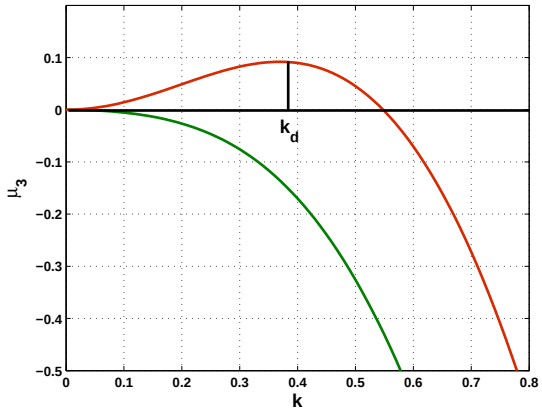

Figure 4.3: **Dispersion curve when** $\bar{c} < c^*$, above the threshold $\zeta v > D\bar{\alpha}$, a band of wavenumbers centred around k_d are unstable (red curve). The green curve represents the growth rate vs k below the threshold

The existence of the instability is verified numerically by evolving an initially randomly distributed, randomly orientated state according to the equations of motion. Beyond the threshold of stability, the solutions of the equations of motion constitute a square lattice of inward pointing asters.

The above instability arises primarily because of the competition between advection and diffusion of filaments. However, when $\bar{c}$ is greater than c^*, the entropic ordering interactions between filaments become important. When $\bar{c} > c^*$, the eigenvalues μ_1 and μ_3 are both positive for $k = 0$. The disordered phase is therefore *always* unstable and the *local* orientation $|\mathbf{n}|$ saturates to $\sqrt{\bar{\alpha}/\beta}$. With a $k = 0$ instability, it is natural to assume that the final steady state maybe homogeneous and ordered. However, the analysis so far does not make such predictions, and a stability analysis about the homogeneous ordered state will have to be performed.

4.2.4.2 Stability about the homogeneous ordered state

We start with the homogeneous ordered state and $\bar{c} > c^*$. In this case,

$$\mathbf{A} = \begin{pmatrix} -Kk^2 - \delta K k_x^2 - i\lambda k_x - 2\bar{\alpha} & -\delta K k_x k_y & ik_x\zeta \\ \delta K k_x k_y & -Kk^2 - \delta K k_y^2 - i\lambda k_x & ik_y\zeta \\ -ik_x v & -ik_y v & ik_x v - D_f k^2 \end{pmatrix} \quad (4.10)$$

We proceed by writing down the eigenvalues of $\mathbf{A}$ for the purely bend ($k_y = 0$) and purely splay ($k_x = 0$) distortions to leading order in wavenumber.

Bend, $k_y = 0$

$$\begin{aligned} \mu_1 &= -Kk_x^2 - i\lambda k_x + ... \quad (4.11) \\ \mu_2 &= -2\bar{\alpha} - k_x^2(K + \delta K + \frac{\zeta v}{2\bar{\alpha}}) - i\lambda k_x \\ \mu_3 &= k_x^2(\frac{\zeta v}{2\bar{\alpha}} - D_f) - k_x^4 \frac{\zeta v}{\bar{\alpha}^3}(2\bar{\alpha}(-D_f + K + \delta K) + (v - \lambda)^2 + \zeta v) \\ & \quad -ik_x v \end{aligned}$$

Splay, $k_x = 0$

$$\begin{aligned} \mu_1 &= -2\bar{\alpha} - Kk_y^2 \quad (4.12) \\ \mu_2 &= -\sqrt{\zeta v}k_y - \frac{D_f + K + \delta K}{2}k_y^2 \\ \mu_2 &= \sqrt{\zeta v}k_y - \frac{D_f + K + \delta K}{2}k_y^2 \end{aligned}$$

In the absence of contractility ($\zeta v = 0$), the homogeneous ordered state is stable. The first instability that comes into play as soon as contractility is turned on ($\zeta v > 0$) is composed of a band of distortions centred around the splay distortion ($k_x = 0, k_y = k_o$)(4.12), with

$$k_o = \frac{\sqrt{\zeta v}}{(D_f + K + \delta K)} \quad (4.13)$$

4.2.5 Numerical Results and the zero temperature phase diagram

We will henceforth refer to inward pointing asters as "asters" and outward pointing asters as "anti-asters". Numerically solving the equations of motion, we see that the instability at ($\zeta v > 0$) leads to the formation of a family of 'boojums' (Figure 4.4 (a)), a phase where a large fraction of the filaments align along the ordering direction $\hat{e_x}$. As ζ is increased to greater than $\sim v/4$, a transition between the boojum phase and an 'aster street' (Figure 4.4 (b)) is observed. This phase is a mixture of asters and the ordered phase, where 'streets' formed by ordered filaments separate now self-anchored asters. Increasing ζ further leads to a larger proportion of filaments residing in asters, until regions with local order finally disappear. Beyond a critical value $\zeta_c/K = 4$, we move in to a square lattice configuration of asters (Figure 4.4 (c)).

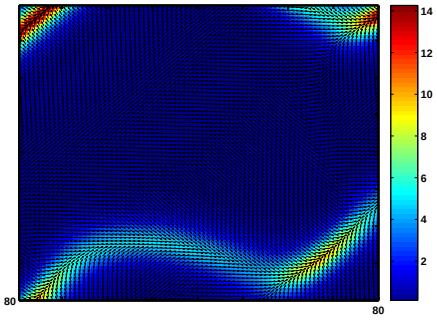

(a) A 'boojum' configuration when $D_f = 20, \zeta/K = 0.02, v = 4$

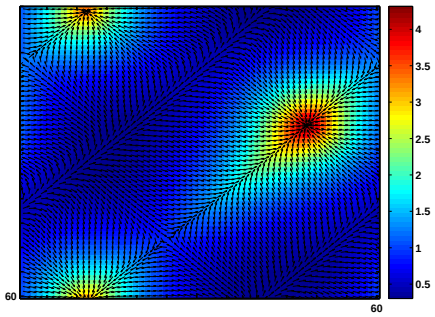

(b) An 'Aster street' when $D_f = 20, \zeta/K = 2.5, v = 1$

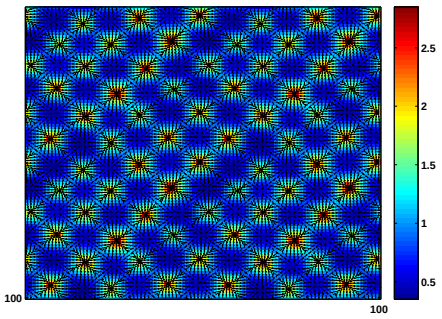

(c) A 'lattice of asters' when $D = 5, \zeta/K = 6, v = 1$

Figure 4.4: **The different zero-temperature phases**

The boojum and the aster street are both moving phases, with filaments moving with respect to the solvent in an ordering direction (say $\hat{e}_x$). The drift velocity of the filaments with respect to the fluid $\langle c\mathbf{n} \cdot \hat{e}_x \rangle$is non zero in both these phases. The lattice of asters, in contrast, is a stationary phase characterized by a zero drift velocity. The drift velocity $v_d = \langle c\mathbf{n} \cdot \hat{e}_x \rangle$ is thus chosen as the order parameter for the street-lattice transition. The average drift velocity shows a jump when we move from a boojum to an aster street (Figure 4.5 (a)), reflecting the difference in the symmetry of the two phases. It shows a power law decay $v_d \sim (\zeta - \zeta_c)^\nu$ with a power $\nu \sim 1.7$ as ζ approaches $\zeta_c = 4K$, beyond which it remains zero, indicating the existence of a continuous transition between the street and the lattice.

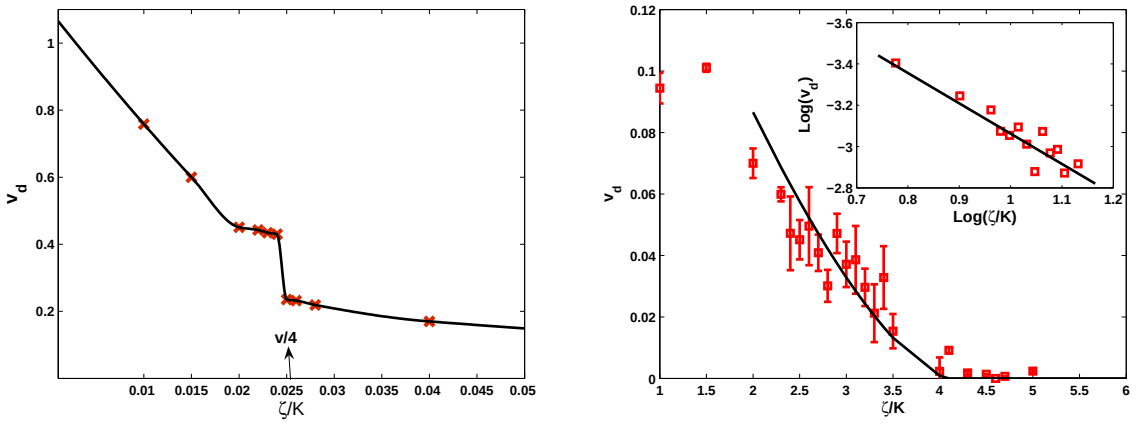

(a) (b)

Figure 4.5: **Velocity $\langle c\mathbf{n}.\hat{e}_x \rangle$vs ζ/K.** (a) At the boojum-street transition, the velocity shows a jump (b) At the street-lattice transition, the velocity shows a continuous power law decay to zero satisfying $v \sim (\zeta/K - 4)^{1.7}$

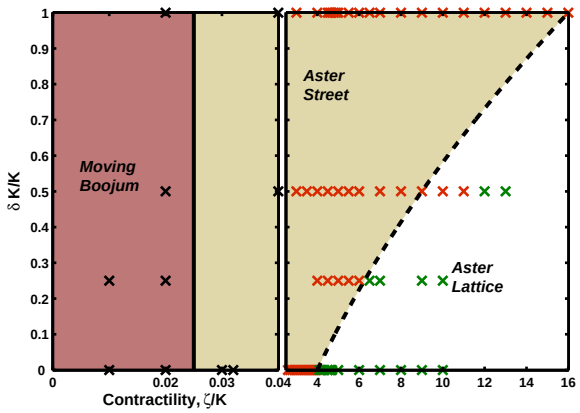

Figure 4.6: **Zero temperature phase diagram** for $K = 10, D = 5$.

4.2.5.1 Boojum-Street Transition

Figure 4.6 is the numerically obtained phase diagram representing the transitions described above, where we have chosen the dimensionless quantities ζ/K and $\delta K/K$ as the axes. At low $\zeta/K = 0.025 \sim v/4$, the boojum-street transition, takes place almost independent of $\delta K/K$. This is a numerical fact, true within our numerical resolution of the parameter ζ/K, which is incremented in steps of 0.01 to obtain the above phase diagram. This independence does however suggest that the transition occurs due to a competition between contributions $\zeta \nabla c$ and $\nabla \cdot (c\mathbf{n})$ - anchoring and advection, which dominate over the distortion terms $K\nabla^2\mathbf{n}$ and $\delta K \nabla(\nabla \cdot \mathbf{n})$ at low wavenumber.

We can understand the stability of an aster qualitatively by making two kinds of perturbations on it, as illustrated in Figure 4.7. The perturbation shown in 'B' changes the position of the core of the aster, producing a net asymmetry. A net flux can towards the right arises due to this asymmetry and this flux is kept in check due to anchoring at the boundary of the aster, pushing filaments back in. However, if the flux exceeds a certain value ($\sim 4\zeta$), the perturbation becomes unstable, leading to the formation of a boojum.

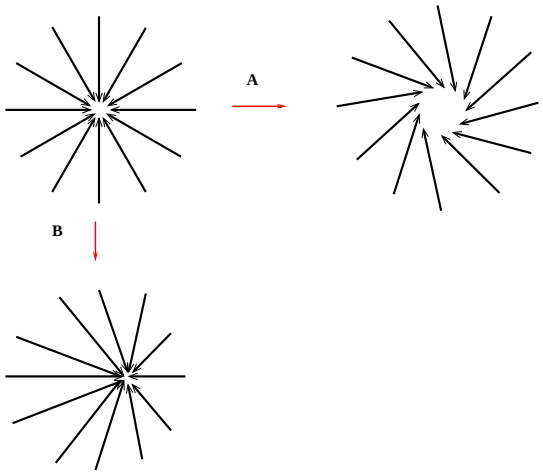

Figure 4.7: **Perturbations of an aster** (A) taking it to a spiral (B) taking it to a boojum

4.2.5.2 Asters-Spirals

To obtain the phase diagram, we have set $\lambda = 0$. Changing this parameter can take us from asters to spirals. Spirals are usually formed when $\delta K/K$ is large [26]. However, in our case, anchoring, being an effect linear in wavenumber, dominates over these terms and we do not obtain spirals, unless $\lambda \neq 0$. Once again, we can qualitatively understand the spiral by viewing it as a perturbation of the aster, represented by 'A' in Figure 4.7. Anchoring tends to align filaments towards the core of the aster, while the λ term serves to align filaments along the flow. At a large λ, we therefore see spiral configurations.

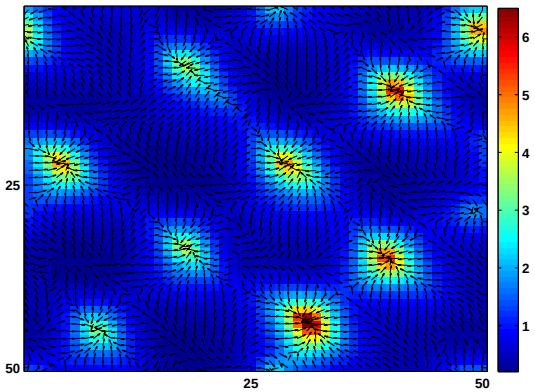

Figure 4.8: **A lattice of spirals** at $D_f = 10, \zeta/K = 10, \lambda = 10$

4.2.5.3 Street-Lattice Transition

The street-lattice transition is reminiscent of the impurity pinning of charge density waves in a superconductor in the presence of an electric field [18]. The velocity of the charge density wave has a nonlinear response to the electric field due to the impurities, and decreases continuously to zero as the field approaches a critical value E_c. Within mean field theory, the velocity varies with the field as $v_{cdw} \sim (E - E_c)^{3/2}$. The "self pinning" of asters, therefore shares some commonality with this phenomenon, and mean field theory should be sufficient for our purposes. The transition occurs when the distance between the asters (Figure 4.9), set by the linear stability value $1/k_o$ is of the order of the bend correlation length $\sqrt{K}$. In the lattice of asters phase, the distance between the asters varies inversely with $\sqrt{\zeta}$, as expected from the linear stability analysis. The transition warrants further investigation, but we do not go into it in this thesis.

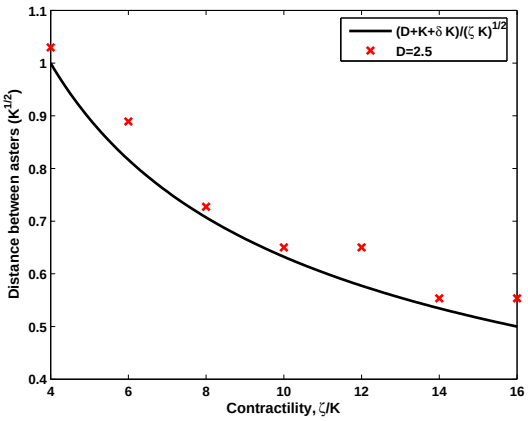

Figure 4.9: **Distance between asters** for $K = 10, D = 5$.

4.2.5.4 Size of the aster

The concentration profile in a single aster is obtained by balancing the advective flux of filaments towards the core by the diffusive flux

$$vc(r)\mathbf{n} \quad = \quad D_f \nabla c \tag{4.14}$$

The solution of this equation in plane polar coordinates is $c(r) = c(0)e^{-vr/D_f}$. The size of

the aster is therefore set by the length D_f/v, which is a result borne out by the numerics as well. Figure 4.10(a) is a log linear plot of the concentration profile of filaments centered around the aster core, and shows an exponential decay. Fig 4.10(b) is a plot of the slope of (a) at different values of D_f, coinciding with the analytical value D_f/v.

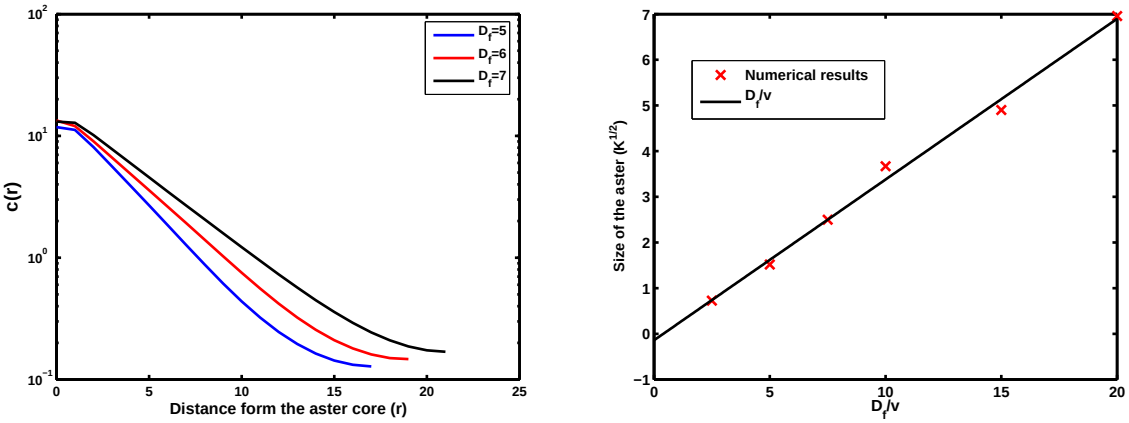

(a) (b)

Figure 4.10: **Aster Characteristics** (a) A log linear plot of the concentration profile from the centre of the aster for various values of D_f, shows that the concentration falls exponentially from the aster core.(b) The size of the aster varies linearly with D_f, as expected.

4.2.5.5 Instability of vortices and anti-asters

The advection - self-anchoring coupling renders both vortices and outward pointing asters unstable. This is easy to see from simple arguments :
An anti-aster with uniform concentration has a configuration that leads to the advection of filaments away from the its core. This leads to a lack of filament concentration in the region occupied by the core, and hence a stable anti-aster is never found (Figure 4.11(A)). A small perturbation to the orientation of a uniform vortex (Figure 4.11(B)), causes the concentration of filaments to be advected towards the core of the aster. Self anchoring further aligns filaments along the gradients of concentration, and the eventual steady state is either a spiral or an aster.

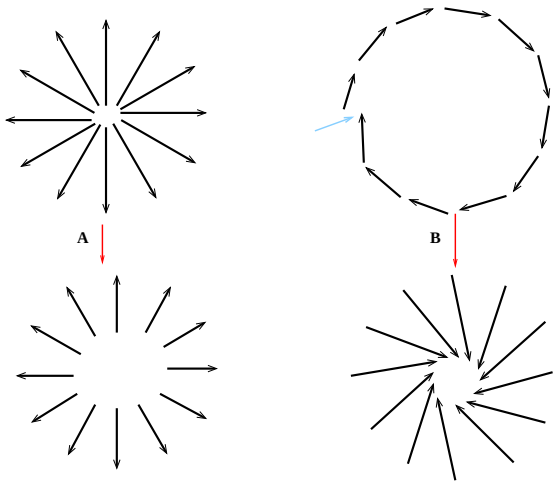

Figure 4.11: **Instability of vortices and anti-asters** (A) Filaments at the core of the anti-aster are advected away from the core, rendering an anti-aster unstable (B) Small perturbations (blue arrow) towards the core of a vortex, destabilizes the vortex, leading to the formation of either a spiral or an aster.

4.3 In the presence of noise

The lattice of asters is a two dimensional solid where each 'atom' of the solid is an aster. At a finite temperature, the vibrational levels of the individual atoms of a solid are excited and they oscillate about their mean position. At a critical value of the noise, the Lindemann criterion for melting of solids states that when the average root mean square displacement of the atoms is of the order of their separation, the solid melts and the atoms are freed from their mean positions. However, we have a solid where each 'atom' is made up of a number of filaments. In the presence of noise, some of the filaments are freed from their native aster and enter the melt in between the asters. In particular, at a critical value of the noise amplitude (temperature), an entire aster can disintegrate. The filaments in the melt have the propensity to transiently re-form aster-like configurations.

4.3.1 The $\zeta - T_A$ phase diagram.

We assume that the noise in concentration equation (4.6) is a conserved noise with an amplitude $\sqrt{A_c}$, with zero mean and a correlation function given by

$$\langle f_c(r,t) f_c(r',t') \rangle = A_c \nabla^2 \delta(r-r') \delta(t-t') \tag{4.15}$$

The orientational noise is also delta correlated with a zero mean and width T_A.

$$\langle f_{\mathbf{n}}(r,t) f_{\mathbf{n}}(r',t') \rangle \quad = \quad T_A \delta(r-r') \delta(t-t') \tag{4.16}$$

The phenomenological parameter T_A is an active temperature, that subsumes in it various external contributions to noise (such as stochasticity in myosin binding-unbinding) that actively change the orientation field. In our numerical treatment, we start with a stable lattice of asters and evolve it to its new steady state in the presence of noise.

At low T_A, we find a phase where the number of asters do not change, and the cores of the asters exhibit vibrational fluctuations. This is referred to as the 'phonon phase'. Although the *number* of asters is constant, the quantity $\langle c \nabla \cdot \mathbf{n} \rangle$, which is a measure of the density of aster-like divergences, decreases progressively as a function of T_A (Figure 4.12 (a)). This is due to a decrease in the concentration of filaments bound to asters, and a corresponding increase, in the bulk. When $T_A > 27$, the asters start to disintegrate and we are no longer in the phonon phase. As elaborated on in the next subsection, the system moves into a realm of remodeling.

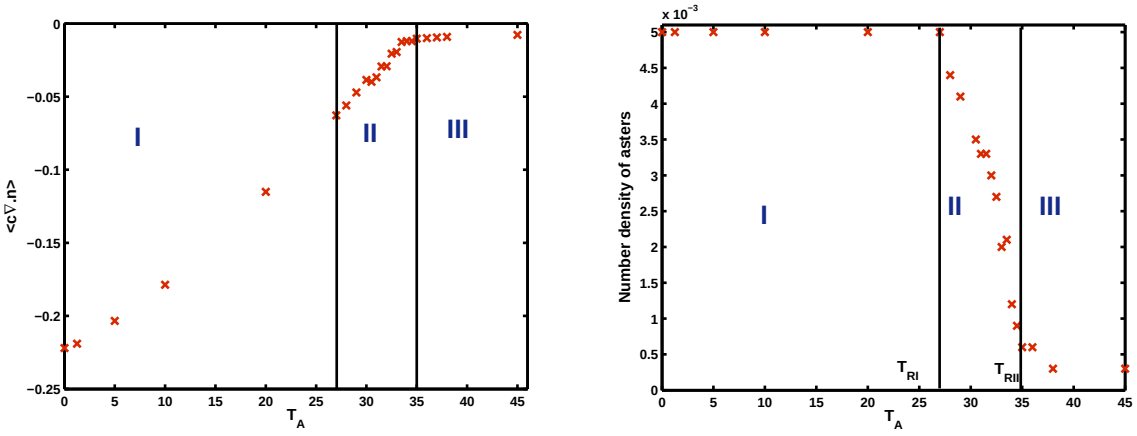

(a) (b)

Figure 4.12: **Noise Changes Bulk Characteristics.** (a) Average aster density vs T_A for $\zeta/K = 10$ (b) Number of asters T_A for $\zeta/K = 10$

4.3.2 Realm of remodeling

In region II of the Figures 4.12 (a) and (b), asters begin to disintegrate and enter the melt. In region III, although all the asters have melted, the aster density is still non zero. We can now ask the following questions:

(1) Can the disintegrated asters reform, and remain in an aster-like configuration for a finite amount of time ?

(2) If they do reform, do they do so in a spatially correlated manner?

In order to answer the first question, we map the formation - disintegration dynamics of asters to a persistence process: the asters are now viewed as quasi-particles, occupying an area of linear dimension $\sim D_f/v$. The quantity $c\nabla \cdot \mathbf{n}$ represents the local density of asters. A local average of this quantity in a box of side $2D_f$ is negative when an aster-like configuration occupies the box. A simple coarse graining procedure can be used to convert the field $c\nabla \cdot \mathbf{n}$ to a binary field b_A of the occupation numbers of asters 0 and 1. A point b_A has a value 1(0) when the average value of $c\nabla \cdot \mathbf{n}$ in a box of length $2D_f/v$ surrounding that point, is $< 0 (\geq 0)$. The time series of each point of the binary map helps us calculate the lifetime of asters. Figure 4.13 contains a sample time series of a point in b_A, showing the disintegration and re-emergence of an aster at that point. From the time series, we can find out of the residence and aggregation time distributions of each point in the binary map. The residence time of an aster is defined as the time for which a point in b_A has a value =1, and the aggregation time is the time for which it has a value =0. The mean residence times of both asters and anti-asters, decreases with T_A(Figure 4.19). Figure 4.14 (Figure 4.15) contain plots of residence(aggregation) time distributions for various values of T_A. At $T_A = 35$, we notice a transition between a residence time distribution that decays as a *power law* (with a power ~ 2.7) to one that decays *exponentially*.

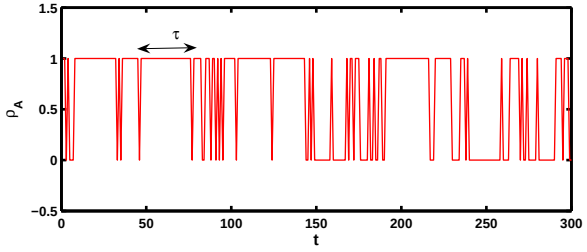

Figure 4.13: **Time series of a representative point in b_A showing formation and fragmentation of an aster**

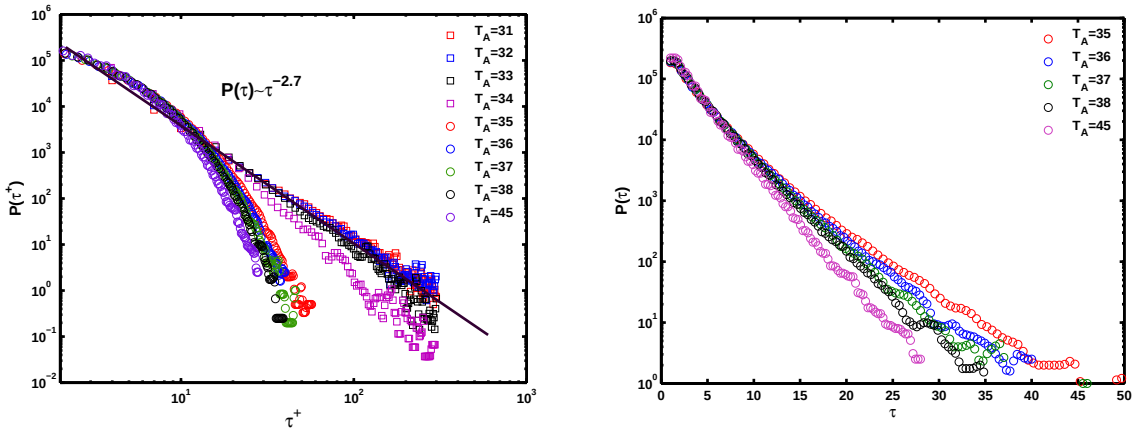

(a) (b)

Figure 4.14: **Residence Time Distributions of Asters.** (a) A log-log plot shows two regimes: a power law regime with a power ~ 2.7(squares) and an exponential regime above $T_A = 35$ (b) A log-linear plot above $T_A = 35$ highlighting the exponential regime.

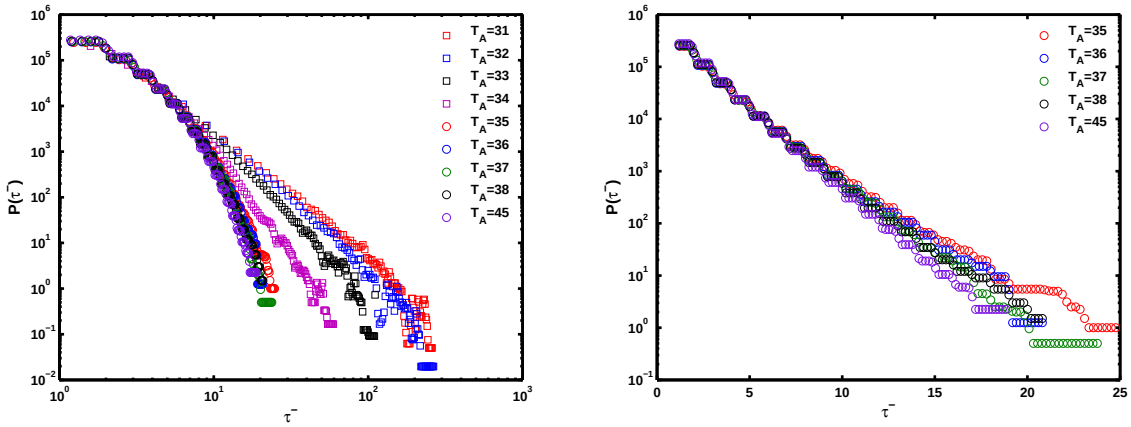

(a)

Figure 4.15: **Aggregation time distributions of asters.** (a) A log-log plot showing a transition from a power law decay (squares) to an exponential decay (circles) at $T_A = 35$ (b) A log-linear plot above $T_A = 35$ highlighting the exponential regime.

To address (2), we calculate the time averaged structure factor $S(\mathbf{k}) = ({}_0\int^{\tau_O} \rho_A(\mathbf{k},t)\rho_A(-\mathbf{k},t)dt)/\tau_O$, τ_o being the time of observation. Figure 4.16 shows the structure factor for various values of T_A. In the phonon phase, as expected we find Bragg peaks corresponding to the reciprocal vectors of the square lattice. As T_A increases moves into Region II, the Bragg peaks persist. In Region III, although indiscernible when $S(\mathbf{k})$ is plotted with respect to $|\mathbf{k}|$, the Bragg peaks are visible in a contour plot of $S(\mathbf{k})$ (Figure 4.16 (b)). Tetratic correlations are therefore present in both regions of remodeling, indicating a high spatial sensitivity in the formation of asters.

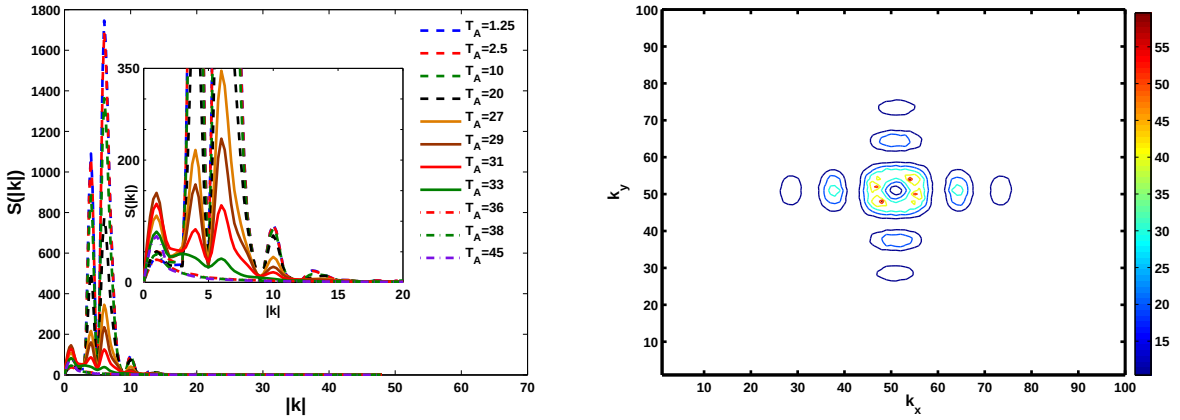

(a)

Figure 4.16: **Structure factor at various** T_A (a)$S(|\mathbf{k}|)$ for various values of T_A showing Bragg peaks (b) Contour plot $S(k_x, k_y)$ for $T_A = 45$

4.3.3 Discussion

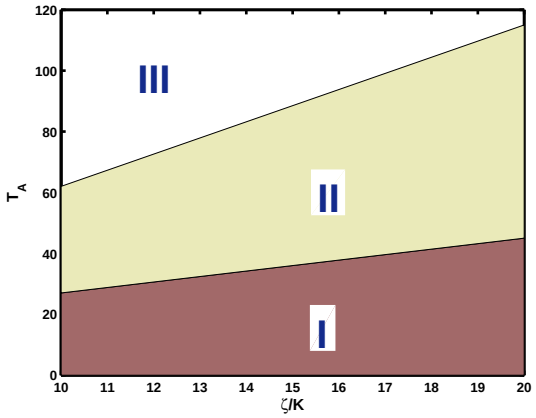

Figure 4.17: $\zeta - T_A$ **phase diagram**

With these results, we can now understand the $\zeta - T_A$ phase diagram. In Region I, we see only phonon fluctuations of the cores of the asters, on average the asters can be considered static. In Region II of the phase diagram, although disintegration takes place, a number of static asters still occupy the bulk, some of which are very long lived, as indicated by the power law decay of $P(\tau)$. In this concentrated system, (route A of Figure 4.18), reappearance of a new aster will be sensitive to the contractile interactions between asters. Reappearance will only occur in a previously occupied region.

In the region III, all the static asters have melted away, and all the existing ones participate in rapid disintegration-reappearance. Reappearance of an aster will still be sensitive to contractile interactions, but need not occur in a previously occupied region. No positional correlation is therefore present, however contractile interactions between asters makes them locally square ordered, giving rise to long range orientational correlations.(route B of Figure 4.18)

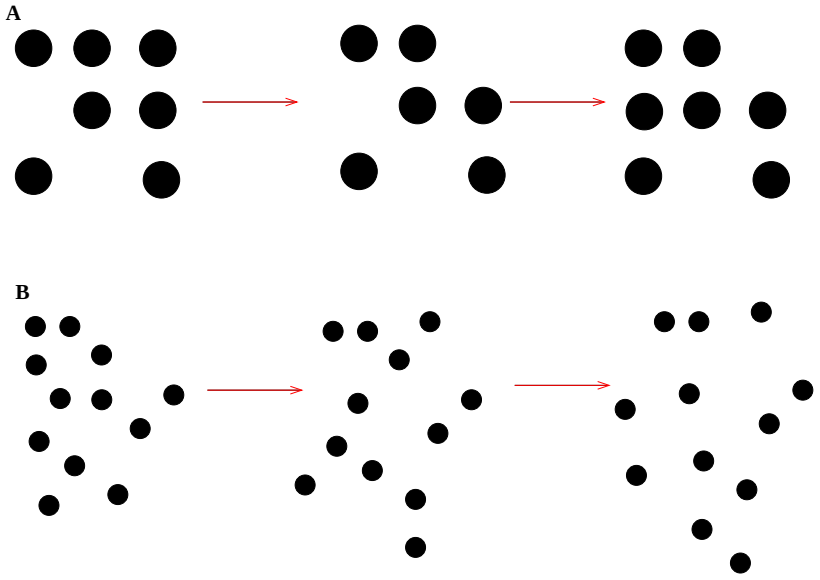

Figure 4.18: **Aster Formation and Fragmentation** (A) In the power Law regime (B) In the exponential regime (explanation in the text)

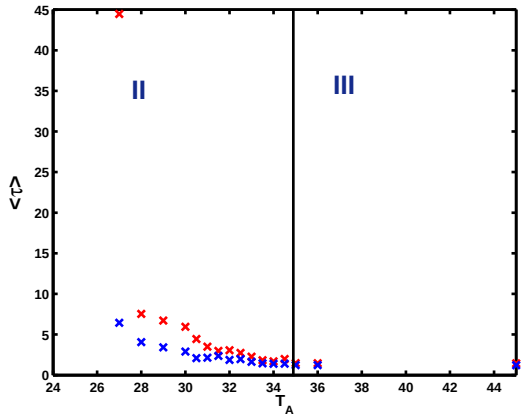

(a)

Figure 4.19: **Mean residence and aggregation times of asters as a function of** T_A

4.4 Back to GPI-APs

4.4.1 Inert, passive and active molecules

We now collate all our results and try to understand how actin modulates molecular composition on the plasma membrane. The molecules encountered in chapter 3 were responsible for recruiting different architectures of actin at the membrane, and are presumably affected by the active stresses generated by actin. In chapter 2, we showed that nanocluster density is a function of actin, and in addition saw that unsaturated lipids are unaffected by actin. This leads us to categorize the membrane molecules as

1. **Active**: The molecules control the local actin architecture. Once actin is nucleated, the stresses it applies will in turn affect active molecules. Since cholesterol affects the recruitment of actin at the membrane, it can be categorized as an active molecule.

2. **Passive**: They are affected by actin, via indirect interactions, however, they do nothing to modulate actin architecture. We suggest that the GPI-AP, associating with cholesterol via its lipid anchor, is one such molecule.

3. **Inert:** These include transmembrane proteins, too large to feel the forces exerted by actin, and short chain lipids, that do not associate with cholesterol.

4.4.2 Numerical Results

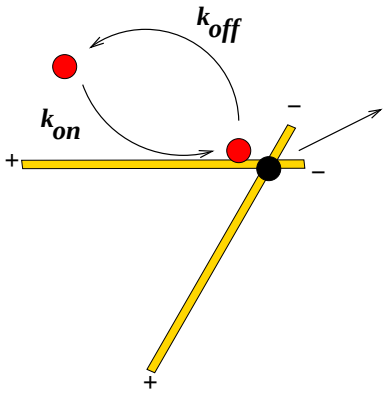

Figure 4.20: **Passive Particle dynamics.** A Passive Particle (in red) hops on and off a cross-linked pair of filaments and is advected along by the filaments

We now hypothesize that the GPI-AP is a 'passive particle'. When bound to a filament, the particle is carried along by the filament current ; when free, it diffuses in the membrane environment with a diffusion coefficient D_ρ. The concentration of passive particles given by $\rho(\mathbf{r},t)$ is composed of concentrations $\rho_b(\mathbf{r},t)$ of particles bound to filaments and $\rho_f(\mathbf{r},t)$ of free particles, whose values come from a mean field rate equation and a local conservation

$$\begin{aligned} \frac{d\rho_f}{dt} &= k_{on}\rho_f c - k_{off}\rho_b \\ \rho_f(\mathbf{r},t) + \rho_b(\mathbf{r},t) &= \rho(\mathbf{r},t) \end{aligned} \tag{4.17}$$

This is consistent with the assumption that the binding-unbinding of particles occurs much faster than advection or diffusion. The fractions of free and bound passive particles are therefore

$$\begin{aligned} \rho_b(\mathbf{r},t) &= \frac{k_{on}c(\mathbf{r},t)}{k_{on}c(\mathbf{r},t)+k_{off}}\rho(\mathbf{r},t) \\ \rho_f(\mathbf{r},t) &= \frac{k_{off}}{k_{on}c(\mathbf{r},t)+k_{off}}\rho(\mathbf{r},t) \end{aligned} \tag{4.18}$$

The passive particles obey a continuity equation similar to (4.6), where the total passive particle current comes from advective ($\rho_b\mathbf{n}$) and diffusive ($D_\rho\nabla\rho_f$) contributions

$$\partial_t\rho = -\nabla\cdot(\rho_b v\mathbf{n} - D_\rho\nabla\rho_f) + f_\rho \tag{4.19}$$

$\mathbf{f}_\rho$ is a conserved noise consistent with the fluctuation dissipation theorem

$$\langle f_\rho(r,t)f_\rho(r',t')\rangle = (2k_BTD_\rho/\eta)\nabla^2\delta(r-r')\delta(t-t') \tag{4.20}$$

This equation is numerically evolved on a lattice of asters, at different passive particle duty ratios ($K_d = k_{on}\bar{c}/(k_{on}\bar{c}+k_{off})$) and at different active temperatures T_A. The passive particles are assumed to diffuse about 50 times faster than the filaments (D_ρ/D_f=50). The model is able to reproduce some of the features of GPI-APs on cell membranes.

4.4.2.1 Scales

According to our model, the formation of a GPI-AP 'cluster' comes from the localization of molecules of the core of the aster. From the numerics, we find that a patch with a high ρ, occupies each aster core. Closer to the core, particles are close enough to each other for FRET to occur, and away from the core, the particles are independent monomers.

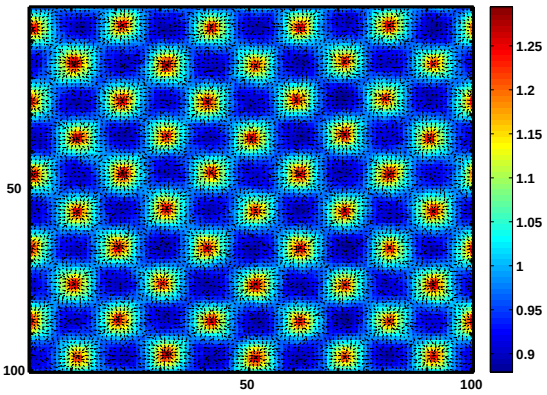

Figure 4.21: **Colocalization of clusters and the aster core.** $D_f = 5, \zeta/K = 10, T_A = 15$

To calculate the size of the patch, ρ is converted to a binary map b_c of zeros and ones where $b_c = 1$ if the density exceed an arbitrary cut off ρ_m, 10% larger than the mean density ($\rho_m = 1.1\bar{\rho}$). Any volume element with a density less than ρ_m has only monomers. This procedure sets a baseline patch size of $\sim 0.2v/D_f$ at zero K_d, where clustering of molecules is a random thermally driven process. As K_d increases, the size of the patch increases sigmoid-ally until it saturates at the size of the aster. As T_A increases, the patch size decreases with a slope that seems to be characteristic of each of the phases of remodeling. Region III in particular, shows a slow decrease in the patch size until at high values of noise, it becomes undetectable.

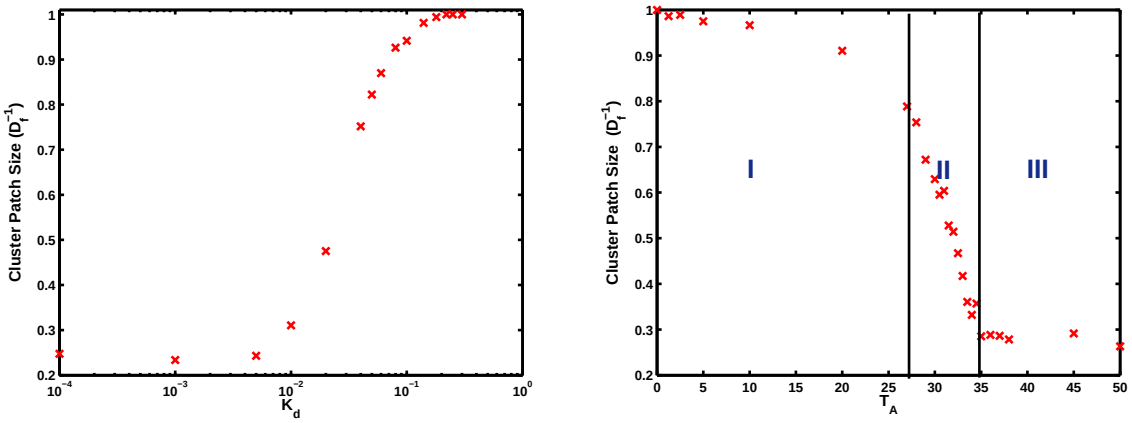

(a) (b)

Figure 4.22: **Size of the cluster** (a) as a function of duty ratio K_d(b) as a function of the noise strength T_A

4.4.2.2 Single Point Distributions

The steady state distributions of density values of each point show the existence of exponential tails at the high density end. The prominence of the tail increases as K_d increases, and decreases with increasing T_A. The distribution of anisotropy, being a linear combination of the monomer density $\rho_m$and the cluster density ρ_c ($A = A_m\rho_m + A_c\rho_c = A_m\rho_m + A_c(\rho - \rho_c)$), is expected to follow the same trend as $P(\rho)$.

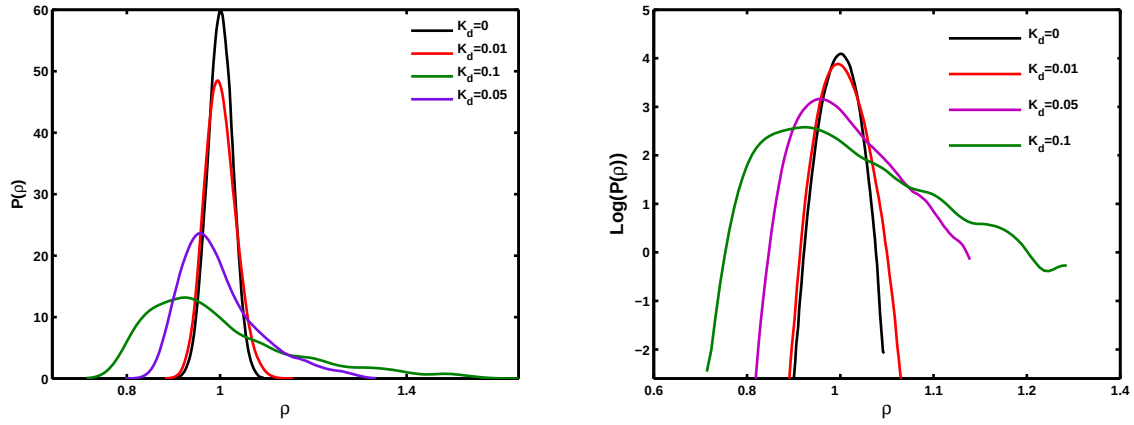

(a) (b)

Figure 4.23: **Single Point Distributions of Passive Particle Density at various Duty Ratios,** shows exponential tails whose prominence increases with increasing K_d

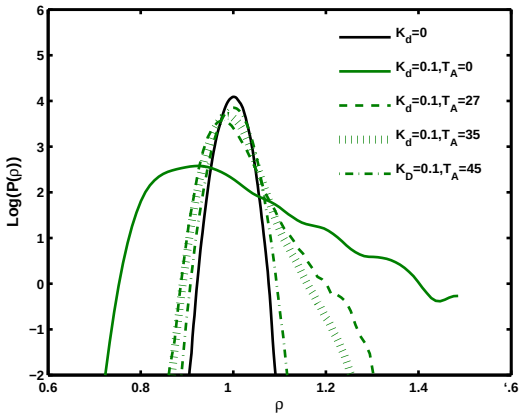

Figure 4.24: **Single Point Distributions of Passive Particle Density at various values of T_A,** shows that the prominence of the exponential tails decreases with increasing noise.

4.4.2.3 Cluster-Monomer interconversion

Switching between high density and low density of the passive particle is due to the combined action of random thermal diffusion and the clustering effect of asters. The dynamics of aster remodeling in the presence of noise, is therefore reflected in the inter-conversion of clusters and monomers. To find the rates of inter-conversion, we analyze the time series of every point in b_c(as defined in section 4.4.2.1). Figure 4.25 shows a sample time series, where the presence/absence of a cluster is dependent on the presence/absence of an aster.

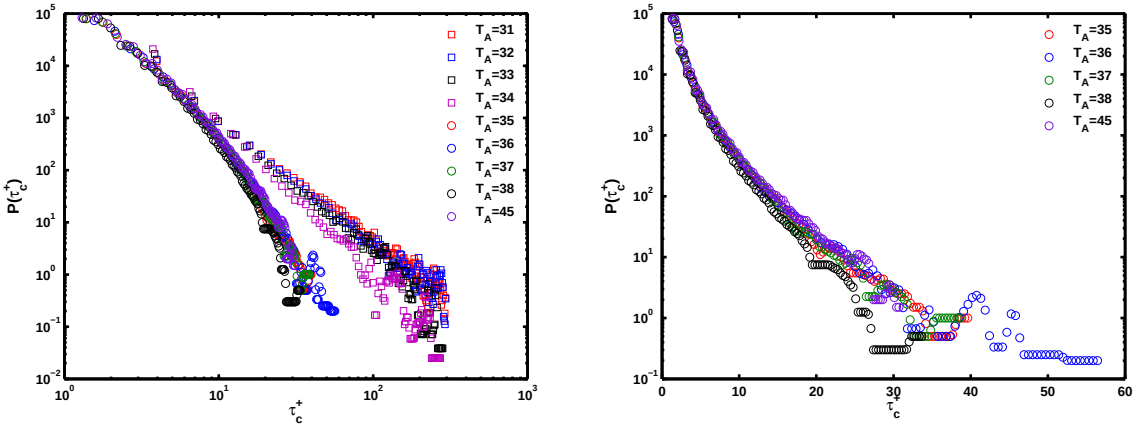

Figure 4.26: **Residence time distributions of clusters**. (a) A log log plot showing a transition from a power law decay for $T_A < 35$ (squares) to an exponential decay (circles).(b) A log-linear plot of the distributions above $T_A = 35$

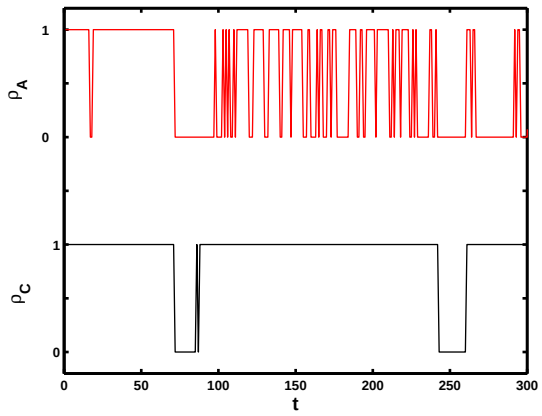

(a)

Figure 4.25: **Time series of a cluster** (black) and its corresponding aster (red), shows that the aggregations and fragmentation of a cluster depends follows the aggregation and fragmentation of the aster.

As in the case of asters, we go on to compute the residence and aggregation time distributions of the clusters (Figures 4.26 and 4.27).

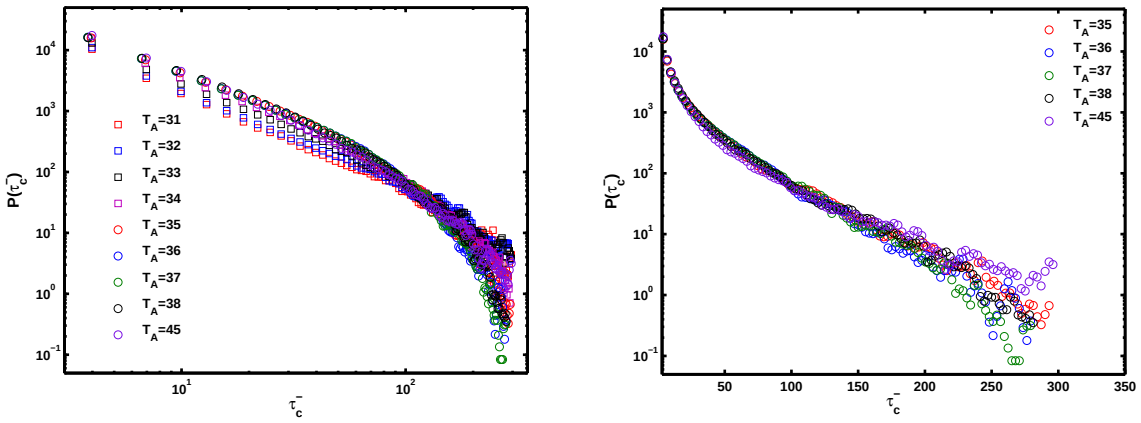

Figure 4.27: **Aggregation time distributions of clusters.** (a) A log-log plot of the aggregation time distribution shows a power law decay for $T_A < 35$ (squares) and a deviation from the power law distribution above this temperature (circles). (b) A log linear plot of the distributions above $T_A = 35$.

Predictably, the residence time distributions of a cluster follow those of asters. We are now in a position to plot an Arrhenius curve for the aggregation and fragmentation rates of the clusters. The rate of aggregation k_a (fragmentation k_f) of a cluster is the inverse of the average residence time of 0(1)'s in the map b_c. In the Arrhenius plot obtained (Figure 4.28) we clearly see a switching behaviour between two phases, separated by the remodeling temperature T_{RII}. In region II, corresponding to the power law regime of the asters, clusters begin to fragment, while the formation of clusters is a much slower process, as in the case of asters. As we move into region III, the formation and fragmentation rates are of the same order, and we get a situation where cluster formation overcomes fragmentation. Note the characteristic slopes of the two regions, reflecting the two remodeling phases of the aster.

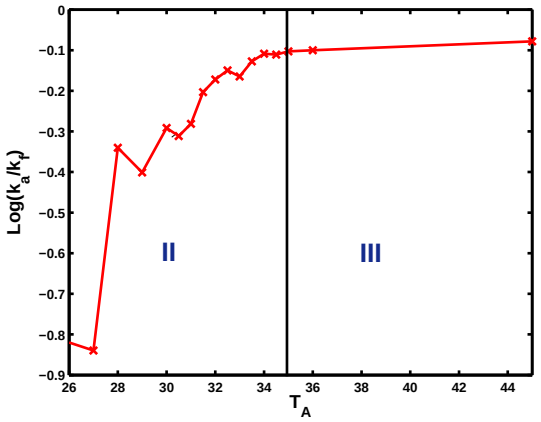

Figure 4.28: **Arrhenius curve.** In the two remodelling regimes, the ratio of the formation and fragmentation rates of clusters differ by orders of magnitude.

4.5 Clustering: Advection vs Molecular sequestering

Clustering of passive particles in our model occurs via localization of particles at the core of the aster. We can contrast this situation to clustering that occurs via sequestering of passive particles by a molecule. Consider a molecule 'X', capable of binding upto 'n' passive molecules. The binding-unbinding rates $(k_{on,X}, k_{off,X})$ of the passive molecules onto the particle X is assumed to obey detailed balance. We ask if clustering via passive particles gives the same features that we see in the experiment. Clearly, the non-Arrhenius behaviour of the binding and unbinding rates will not be exhibited by this model as the rates obey detailed balance.

We now check if this model can reproduce the exponential tails of the nanocluster density. If the particles X are randomly scattered on the membrane, of size L, divided into N sites, the probability of M particles occupying a site is given by a Poisson distribution. Let us assume that in the absence of binding-unbinding, the passive particles are uniformly distributed, and that upon binding, the density of free passive particles does not change considerably. Each of these M particles can bind upto n passive particles. A single passive particle binds to the particle X with a probability $K = k_{on,X}/k_{off,X}$. The number of bound particles per particle 'X' is binomially distributed, and hence the mean number of bound passive particles is nK. With this we can find the probability of finding B bound particles at a given site

$$P(B) \;=\; nKP(M) \tag{4.21}$$

With this simple argument it is easy to see that the passive particle density, has a probability distribution $P(B)$, a Poisson distribution with Gaussian tails. Therefore, unless the particle X is also affected by actin, such a model cannot qualitatively reproduce the features seen in our experiments.

4.6 Evidence for asters at micron scales

Asters of actin have been observed in various contexts, both in vivo and in vitro.

When a T cell meets an antigen presenting cell, an immunological "synapse" forms at the junction between the two. In a recent experiment [25], T cells were adhered onto a lipid bilayer containing freely diffusing anti T-cell receptor (TCR) antibodies and its co-receptor ICAM1. Using spinning confocal microscopy, It was found that at the synapse, both the TCR's as well as ICAM-1's show a movement towards a central core (Figure 4.29 A). Speckle microscopy revealed that actin forms a aster like structure, possibly aiding in the coming together of these molecules. The size of the aster is about 10 microns.

Fascin is a bundling protein that passively binds parallel filaments of actin. Solutions of actin, myosin II and fascin, were studied [11]in a range of myosin concentrations. As the myosin concentration was varied, phases characterized as "Actin networks" and "Actin Asters" were found. Once again, the size of the asters was of about of 10 microns. (Figure 4.29 B)

4.7 Conclusions

The dynamics of short filaments in the presence of long static filaments, subjected to active noise, shows a variety of features that can be compared with experiments.

Firstly, the lattice of asters phase obtained in our zero temperature phase diagram gives us a mechanism for the formation of a static cluster. The distribution of the single point passive particle density has exponential tails.

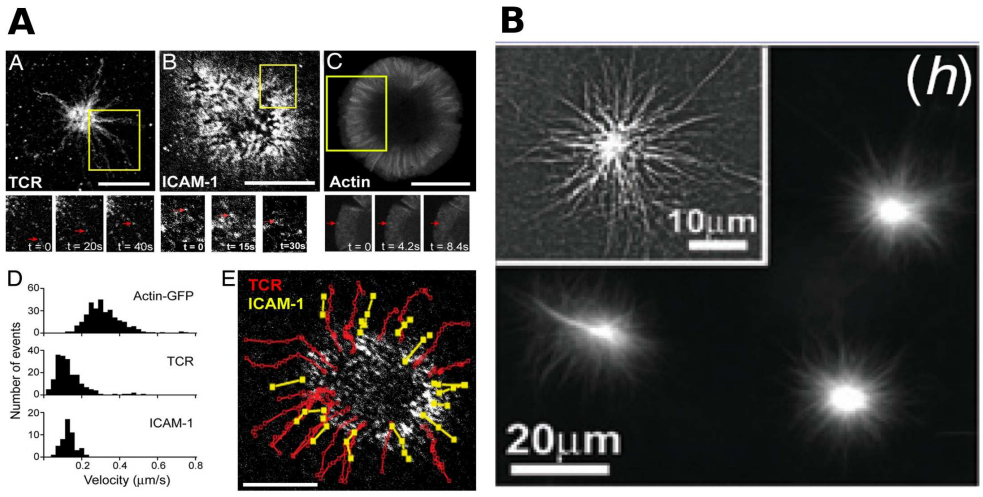

Figure 4.29: **Micron sized Asters.** (A) In vivo: Investigations by kaizuka et al. A-C are the maximum intensity projections of TCR, Icam-1 and GFP-labeled actin speckles respectively. D contains histograms of transport rates of actin, TCR and ICAM-1, while E shows the trajectories of TCR and ICAM-1, moving towards the core of the aster.(Scale bar=10 microns) [25](B) In vitro: A 10 micron sized aster formed in solutions of actin, a passive bundling protein called fascin, and at high concentrations of Myosin II. [11]

As seen earlier, the long static filaments can be treated as a quenched random field, when one studies a patch of membrane much larger than the mesh size. In our theoretical framework, we have treated the effect of these long static filaments in the mean. However, a closer look at 4.5, tells us that fluctuations about the mean can change the strength of the noise $\mathbf{f_n}$. In the experiments presented in chapter 2, time resolved measurements of anisotropy in a small confocal patch contain a portion of the plasma membrane enabled us to measure the rates of fragmentation and formation of clusters, and we found a broad distribution of the rates at each temperature. Viewing the long static filaments as a quenched source of heterogeneity, can explain this broad distribution.

In vitro experiments [11] show that at very high myosin concentration, depolymerization of filaments can occur, seemingly due to the stresses applied by myosin. This provides a mechanism by which the cell can modulate the diffusion coefficients of the filaments, by simply changing their length. The resultant effect is to change the size of the aster. It is possible that the cell makes use of this mechanism for specific purposes.

The presence of asters can enchance rates of chemical reactions between passive particles, as n-body interactions at the cores of the asters become highly probable [15].

In the presence of noise, the asters of short filaments show a rich phase behaviour, frag-

menting and reforming in a manner that is dependent on the active temperature. This behaviour is reflected in the aggregation and fragmentation of clusters, and we obtain an Arrhenius curve similar to the one in chapter 2.

In this chapter we have made qualitative connections with the experiments presented in chapter 2. However, we are yet to extract numbers that will allow us to make quantitative connections and predictions.

The experiments presented in this thesis suggest that the plasma membrane has an apriori architecture: characterized by the fixed fraction of nano clusters, as well as the distribution of nanoclusters. The activity of cortical actin is crucial in maintaining this architecture. The plasma membrane, subjected to the forces exerted by cortical actin, therefore can be thought of as being held in a *non equilibrium steady state*, as opposed to being an equilibrium free-energy minimizing state. The cell is an open system with a plethora of energy transducing machinery. Collective bodies within the cell: membranes, the cytoskeleton, cellular organelles, are all in principle held in an arrangement which does not so much depend on their energetics, as their dynamics.

In chapter 3, we came across two players - CDC42 and ARF1 that can change the architecture of cortical actin. The cell can therefore *regulate* its actively held organization via a number of molecular players. The cell has a complex molecular machinery that helps in regulating the steady state that it is held in. Using this machinery, the cell can also locally modulate both its shape and composition for specfic purposes.

Finally, the cell seems to make use of its actively held steady state for its functionality. GPI-APs, as we have seen, require their peculiar organization for their endocytosis, and for various other functions.

In this final chapter, we have proposed a theoretical model that uses the the physics of active polar filaments to understand the plasma membrane. From this model, and from its concurrence with the results of the experiments presented in chapter 2, we believe that an adequate description of the plasma membrane and surely, all other cellular bodies, comes from a complete consideration of all the forces that they are subjected to.

Bibliography

[1] Alberts B, Johnson A, Lewis J, Raff M, Roberts K, Walter P, *Molecular Biology of the Cell*, Garland (2001)

[2] Doi M and Edwards S F. The theory of Polymer Dynamics, Clarendon Press (1999)

[3] De Gennes P G and Prost J. *The Physics of Liquid Crystals*, Clarendon Press (1993)

[4] Israelachvili J N. Intermolecular and Surface Forces, Academic Press, (1992)

[5] Lakowicz J R, *Principles of Fluorescence Spectroscopy,* Springer (1993)

[6] Nelson P, *Biological Physics : Energy, Information, Life*

[7] Press W, Teukolsky S, Vetterling W and Flannery B, *Numerical Recipes*, 2nd Edition, Cambridge University Press (1992)

[8] Sarasij R C, PhD thesis (2004).

[9] Ahmadi A, Marchetti M C and Liverpool TB, *Phys.Rev.E* **74**,061913 (2006)

[10] Aronson I S and Tsimring L S, *Phys.Rev.E* **71**, 050901 (2005)

[11] Backouche F, Haviv L, Groswasser D and Bernheim-Groswasser A, *Phys. Biol.* **3** 264 (2006)

[12] Cao H, Weller S, Orth J D, Chen J, Huang B, Chen J, Stamnes M and McNiven M A, *Nat.Cell Biol.,* **7**, 483 (2005)

[13] Chadda R, Hancock J, Parton R and Mayor S, *Traffic* **8**, 702 (2007)

[14] Charras G T, Coughlin M, Mitchison T J and Mahadevan L, *Biophys. J.* **94**, 1836–1853 (2007)

[15] Chaudhuri A, Bhattacharya B, Gowrishankar K, Mayor S and Rao,M , *Submitted to Proc.Nat.Acad.Sciences* , (2009)

[16] Chhabra E S and Higgs H N. *Nat. Cell Biol.* **9**, 1110–1121. (2007)

[17] Doherty G J and McMahon H T, *Annu. Rev. Biophys.* **37**, 65 (2008)

[18] Fisher D S, *Phys. Rev. Lett.* **50**, 1486 - 1489 (1983)

[19] Goswami D, Gowrishankar K, Bilgrami S, Ghosh S, Raghupathy R, Vishwakarma R, Chadda R, Rao M and Mayor S, *Cell*, **135**, 1085 (2008)

[20] Gov N S, *Phys. Rev. Lett.* **97** 018101 (2006)

[21] Hancock J F, *Nature Reviews Molecular Cell Biology* **7**, 456-462 (2006)

[22] Hatwalne Y, Ramaswamy S, Rao M and Simha R A, *Phys.Rev.Lett*, **92**, 118101 (2004)

[23] Ikeda W, Nakanishi H, Tanaka Y, Tachibana K and Takai Y. *Oncogene* **20**, 3457 (2001)

[24] Incardona J P Rosenberry TL *Mol Biol Cell* **7**, 613 (1996)

[25] Kaizuka Y, Douglass A D, Varma R, Dustin M L and Vale R, *Proc. Nat.Acad.Sc.* **104**,20296 (2007)

[26] Kruse K, Joanny J F, Jülicher F, Prost J and Sekimoto K, *Phys. Rev. Lett.* **92**, 078101 (2004)

[27] Kumari S and Mayor S, *Nat.Cell Biol.* **10**, 30 (2008)

[28] Lee H Y and Kardar M, *Phys. Rev. E* **64**, 056113 (2001)

[29] Mayor S and Rao M, *Traffic* **5**, 231 (2004)

[30] Meri S, Lehto T, Sutton C W, Tyynel J and Baumann M, *Biochem. J.* **316** (1996)

[31] Mogilner A and Oster G, Biophys.J. **71**, 3030-3045 (1996)

[32] Morone N, Fujiwara T, Murase K, Kasai R, Ike H, Yuasa S, Usukura J and Kusumi A, *Journal of Cell Biol.* **174**, 851 (2006)

[33] Muhuri S, Rao M and Ramaswamy S, *EuroPhys.Lett* **78** 48002 (2007)

[34] Plowman S, Muncke C, Parton R and Hancock J, *Proc. Nat.Acad.Sc.* **102**, 15500 (2005)

[35] Ramaswamy S and Rao M, *New. J.Phys*, **9,** 423 (2007)

[36] Sabhranjanak S, Sharma P, Parton R G and Mayor S, *Developmental Cell*, **2**, 411 (2002)

[37] Sankararaman S, Menon G and Sunil Kumar P B, *Phys. Rev. E* **70**, 031905 (2004)

[38] Sharma P, Varma R, Sarasij R C, Ira, Gousset K, Krishnamurthy G, Rao M and Mayor S, *Cell* **116**, 577-589 (2004)

[39] Sheetz M and Spudich J A, *Nature*, **303**, 31 (1983)

[40] Simha R A, Ramaswamy S, *Phys. Rev. Lett*, **89**, 058101 (2002)

[41] Subczynzki W K and Kusumi A, *Biochimica et Biophysica Acta* **1610**, 231 (2003)

[42] Suzuki K, Fujiwara T, Sanematsu F, Lino R, Ededin M and Kusumi A, *Journal of Cell. Biol.* **177**, 717 (2007)

[43] Suzuki K, Ritchie K, Kajikawa E, Fujiwara T and Kusumi A, *Biophys.J* **88**, 3659 (2005)

[44] Toner J and Tu Y, *Phys.Rev.Lett.* **75**, 4326 (1995)